Static performance of steel slag concrete filled steel square hollow section members

You-Fu Yang[a,*], Feng Fu[b], Yu-Qin Zhang[a]

[a] *State Key Laboratory of Coastal and Offshore Engineering, Dalian University of Technology, Dalian, 116024, China*
[b] *Department of Engineering, School of Science & Technology, City, University of London, Northampton Square, London, UK*

Abstract: The performance of steel slag concrete (SSC) filled steel square hollow section (SHS) stub columns and beams under short-term static loading is experimentally and numerically studied in this paper. Fifteen typical specimens, including 10 stub columns and 5 beams, were tested. The main factors investigated are: mass substitution rate of steel slag aggregate (SSA) [$R_{c(f)}$], which is equal to mass of steel slag coarse (fine) aggregate over that of total coarse (fine) aggregate, and tube width-to-thickness ratio (B/t). The failure modes, relationship between loads and deformations, axial/flexural capacity and axial compressive/flexural stiffness were recorded and analysed. The test results indicate that, the SSC filled steel SHS specimens have similar static performance as the reference composite specimens using ordinary concrete (OC). The variation in the mass substitution rate of SSA mainly leads to the difference in the mechanical factors, and simultaneously the behaviour of stub columns with a smaller B/t is better than that of the corresponding specimens with a larger B/t. A modified compressive stress-strain model of the SSC with the effect of R_c and/or R_f was developed, and finite element (FE) models were further established to investigate the static performance of the SSC filled steel SHS stub columns and beams. The FE models were validated by the experimental results in this study and the existing literature. Finally, the suitable method for the axial/flexural capacity prediction of the SSC filled steel SHS members was recommended.

Keywords: Steel slag concrete (SSC) filled steel square hollow section (SHS); Stub columns and beams; Capacity; Stiffness; Stress-strain model; Finite element (FE) simulation.

*Corresponding author. Tel.: 86-411-8470 8510; Fax: 86-411-8467 4141.
E–mail address: youfuyang@163.com (Dr. You-Fu Yang).

1. Introduction

Steel slag is a by-product of cooling molten substance with dicalcium silicate (C_2S), tricalcium silicate (C_3S), tetra-calcium aluminoferrite (C_4AF) and RO sosoloid as the main components produced in the process of steelmaking, and it accounts for about 15%~20% of crude steel output [1-3]. As the world's largest steel producer, China emits a large amount of steel slag waste every year. Currently, the accumulation of steel slag in China is approaching 1.5 billion tons and keeps increasing by 100 million tons per year; however, the overall utilization rate of steel slag is only about 20%~30% [4, 5]. The discharge of large quantities of steel slag not only causes the waste of resources, but also leads to the land occupation and environmental pollution. Therefore, rational disposal and/or reuse of steel slag is an urgent issue to be solved. The research on the utilization of waste steel slag has been carried out earlier in developed countries, such as Japan, America and Europe, and the utilization rate of steel slag waste in these countries has reached more than 95%. Simultaneously, the above-mentioned countries have established the detailed laws and regulations related to the recycling of waste steel slag, and in general the retreated steel slag is mainly used in road engineering, weak foundation reinforcement, or as backfilling material in engineering [1-5].

Steel slag concrete (SSC) is a new type of construction material produced by partially or completely replacing natural aggregates and/or cement in the ordinary concrete (OC) with steel slag products (i.e. aggregates and powder) [1-3]. Generally, the steel slag aggregate products can be obtained by crushing the steel slag blocks and grinding them into steel slag particles, and their quality should meet the relevant technical standards [6-8] after retreatment. Researching the properties of the SSC to promote its engineering application can not only make the waste steel slag resources be reused, but also tackle the pollution of environment and occupation of land caused by steel slag stockpiling. The SSC technology is one of the effective measures to develop green concrete and realize the sustainable development of building, resources and environment, and has become one of the hot spots and frontier problems in engineering and academic circles [1-4]. In recent years, some fundamental studies have been carried out on the steel slag aggregates (SSAs), and mechanical properties as well as durability of the SSC [1-3; 9-10], and the achievements indicate that, in general, the SSC has the advantages of good mechanical properties and durability, while the disadvantages of the SSC include thermal/electrical conductivity, heavy weight, poor stability, and so on. At present, the limited research cannot guarantee the reasonable engineering application of the SSC yet, and due to the lack of technical regulations or standards related to the SSC structures, the SSC is still very rare for the structural members in civil engineering.

Similar to concrete filled steel tube (CFST) [11], pouring SSC into steel hollow section to form SSC filled steel tube can always keep the core SSC confined and protected by the steel hollow section, and can effectually improve the worse soundness of the SSC by interacting between steel hollow section and its core SSC [12]. As a result, the SSC filled steel tube, a new type of composite member, has attracted certain concern in the academic world, but the study on the structural performance of the SSC filled steel tube is still in the initial stage [12-15]. The summary of experimental studies on the SSC filled steel tube members is presented in Table 1. It can be found that, the roles of steel slag products in the core SSC include: cement, steel slag coarse aggregate (SSCA) and steel slag fine aggregate (SSFA), and the studies mainly focus on the compressive behaviour and the bond performance of composite members with circular section. Moreover, Luo et al. [16] experimentally investigated the hysteretic responses of composite columns containing ferronickel slag, and Feng et al. [17] proposed and experimentally studied the physical and mechanical properties of a new type of structural member, i.e. SSC filled fibre reinforced polymer (FRP) tube. Currently, only Yu et al. [12] conducted finite element (FE) simulation on static behaviour of the SSC filled steel tube stub columns; however, the constitutive model of the core SSC was the same as that of the concrete core in the CFST.

To sum up, the research on the static behaviour of the SSC filled steel tube members with square section is still rare and limited, which indicates that further tests, theoretical and numerical modelling are needed in this field to guide the engineering application. Therefore, the main objectives of this paper are: first, to reveal the influence of parameters on the axial compressive and flexural behaviour of typical SSC filled steel square hollow section (SHS) specimens and their counterparts with the OC;

second, to present a strength prediction method of the SSC and a modified constitutive model of the core SSC; third, to conduct numerical simulation on the static behaviour of the SSC filled steel SHS stub columns and beams; and eventually, to discuss the method capable of predicting the axial/flexural capacity of the SSC filled steel SHS members.

2. Experimental research

2.1. Specimen information

Ten stub column specimens and five beam specimens, including SSC filled steel SHSs and the corresponding square CFSTs, were tested, and both SSCA and SSFA were considered. Fig. 1 shows the cross-section of the specimens, in which t and B are wall thickness and overall width of steel SHS, respectively. The specimen length (L) of stub columns and beams were equal to $3.0B$ and $10.0B$, respectively. The experimental parameters of the stub column specimens included mass substitution rate of SSA (R_c and/or R_f) and tube width-to-thickness ratio (B/t), while the unique parameter for beam specimens was mass substitution rate of SSA (R_c and/or R_f), in which R_c and R_f equal to the mass of SSCA and SSFA over that of total coarse aggregate and fine aggregate, respectively. The information of the specimens is given in Tables 2 and 3, where $f_\mathrm{cu,c(b)}$ is cubic compressive strength of concrete when conducting test of composite stub columns (beams), f_y is yield strength of steel tube, K_s is axial compressive stiffness of stub columns, K_b is flexural stiffness of beams, $N_\mathrm{u,e}$ and $N_\mathrm{u,fe}$ are axial capacity of stub column specimens obtained by experiment and FE simulation respectively, and $M_\mathrm{u,e}$ and $M_\mathrm{u,fe}$ are flexural capacity of beam specimens acquired by experiment and FE simulation, respectively.

The outer tube of the stub columns was produced by welding two unequal-limb steel channels using the butt welds, which were made through bending one steel plate of fixed length, while the outer tube of the beams was cut from a cold-formed steel SHS. In addition, two square steel endplates were welded to both ends of each tube, and for the stub column specimens four pairs of stiffeners were welded to one endplate and the adjoining tube wall at the same time to ensure uniform application of axial compressive loads. When one endplate was welded to the tube bottom, the steel tube was placed vertically for concrete core placement. After concrete curing for two weeks, the steel tube at the top of specimen was grinded to be flush with its concrete core to ensure the collaborative bearing of them, and then the other endplate together with stiffeners (if any) were welded to the steel tube. The fillet welds were used while performing welding between the steel tube and the endplate together with the stiffeners (if any).

2.2. Material properties

The steel slag used in the preparation of the SSC was the by-products from converter steelmaking, and had experienced two years of settlement. The steel slag products were manually screened into SSCA of particle size from 5 mm to 20 mm and SSFA of particle size less than 5 mm. The measured chemical compositions of steel slag together with cement used in this study are listed in Table 4. It can be seen that, the chemical compositions of the steel slag are generally similar to those of the cement [1-3].

The physical properties of SSAs and natural aggregates were tested, and the results are listed in Table 5, where NCA and NFA represent natural coarse aggregate (limestone crushed stone) and natural fine aggregate (river sand), respectively. It can be seen that, the SSAs have greater apparent density, bulk density and water absorption rate than the corresponding natural aggregates, which is similar to current available experimental results. Moreover, the crushing index of SSCA is about 50% of that of NCA, and SSFA has a slightly higher fineness modulus than NFA. The grading (measured by what proportion of the aggregate, by mass, passes through different sized sieves) of different kinds of aggregates is demonstrated in Fig. 2, and the upper and lower limits of total passing percentage in the specifications [6-8] are also included. As can be observed from Fig. 2, with the change of sieve size, the total passing percentages of SSAs are different from those of natural aggregates to some extent; however, the total passing percentages of the two kinds of aggregates are generally within the upper and lower limits prescribed by the specifications.

One type of ordinary concrete (OC) and four types of steel slag concrete (SSC) with different mass substitution rate of SSA (R_c and/or R_f) were prepared, and the mix proportion of concrete is listed in Table 6. Considering the higher water absorption rate of the SSAs, the mixing time of the SSC was

30s longer than that of the OC, so that SSCA and/or SSFA absorbed water fully and mixed evenly. Other materials used in concrete mixing were: P.O42.5 cement, fly ash and polycarboxylic acid superplasticizer as water reducer. The workability of the fresh concrete was mainly obtained by the slump tests, and at the same time, a number of cubes and prisms were prepared while pouring the concrete into the steel SHS of the composite specimens. The performance of concrete is also given in Table 6, in which $f_{\mathrm{cu,28}}$ is cubic compressive strength at 28 days, and E_{c} is modulus of elasticity. It can be observed from Table 6 that, four kinds of SSC have similar working performance as the OC; however, compared with the relevant OC, four types of SSC have higher cubic compressive strength and modulus of elasticity due to lower crushing index (i.e. higher strength) and coarser surface of SSAs than those of natural aggregates. These experimental results are also found in previous studies [1-3, 9, 10]. Moreover, axial deformations of concrete prisms were also measured using a specially designed device. The results showed that, the expansion components in the steel slag (mainly RO sosoloid) were obviously reduced after two-year settlement, which makes the deformation development of the SSC similar to that of the OC, that is, the shrinkage was the deformation of all concrete prisms. In general, the shrinkage of the SSC is smaller than that of the relevant OC as the SSAs possess higher strength and/or expansion than the natural aggregates. After 50 days of measurements, the shrinkage of the OC is -404×10^{-6}, while the shrinkage of the SSC with R_{c}=50%, R_{c}=100%, R_{f}=50% and R_{c}=R_{f}=50% equal to -378×10^{-6}, -346×10^{-6}, -258×10^{-6} and -326×10^{-6}, respectively. Similar results have also been observed in the tests introduced in [18-20].

The tensile properties of steel sections were obtained using the standard coupon test. The coupons were cut directly from the flat portion of the finished steel SHS of the composite specimens, and the average values of measured results are listed in Table 7.

2.3. Test set-up and measurement

For stub column specimens, the axial compressive loads were applied through a 5000 kN compressive tester, and the test set-up and measurement are demonstrated in Fig. 3(a). To collect overall axial displacements, four displacement transducers were symmetrically placed on lower platen of the tester, and to monitor the development of typical longitudinal strains and the corresponding transverse strains at half-height section, eight pairs of strain gauges were symmetrically arranged on the tube outer wall. The loading protocols included: 1) when the load was less than 90% of the estimated axial capacity (N_{uc}) using the FE model for the reference CFST specimens [11], the load was applied at a rate of 0.5 kN/min; and 2) when the load was greater than $0.9N_{\mathrm{uc}}$, the axial displacement was applied at a rate of 0.1 mm/min. After the load dropped to half of the peak load or the axial displacement reached 20 mm, the tests were stopped.

For beam specimens, a four-point bending test device was specially designed, and the test set-up and measurement are indicated in Fig. 3(b), where L_{e} is the effective span after deducting the distances between the lower support and the end from the total length, and the vertical loads acting on the mid-span of reaction beam were applied by a hydraulic jack with a capacity of 1000 kN. To detect the overall development process of vertical displacements, five displacement transducers, including two located directly above the lower support while acting on the upper surface, two located at the quarters on the lower surface and one at the mid-span position while acting on the lower surface, were arranged for each specimen. To record the variation of longitudinal and transverse strains at representative locations, twelve strain gauges were arranged on the outer surface of the steel tube at the mid-span section. The loading protocols were: 1) when the external load was lower than 80% of the vertical load corresponding to the estimated flexural capacity (P_{uc}) using the FE model for the reference CFST specimens [11], each level of the vertical load was 10% of P_{uc}, and 2) when the external load was higher than $0.8P_{\mathrm{uc}}$, the vertical displacement was applied at a rate of 1.2 mm/min. The tests were stopped when the tensile fracture of outer steel SHS occurred, or the mid-span deflection exceeded 80 mm.

2.4. Experimental results and discussion

2.4.1. Overall performance and failure modes

The observation of whole testing process demonstrated that, generally, the development of deformations and destruction characteristics of the SSC filled steel SHS specimens were similar to those of the corresponding composite specimens with the OC.

Fig. 4(a1) shows overall failure modes of the stub column specimens. Generally, primary local buckling (denotated by an arrow) of the tube walls together with the corners of the steel SHS appear as an almost complete ring band, and the secondary local buckling of individual tube walls also occurs in most specimens. At the same time, the maximum out-of-plane displacement caused by the primary local buckling area is greater than that of the secondary local buckling area. Moreover, under the same R_{c} and/or R_{f}, the specimens with a lower B/t have a smaller out-of-plane displacement in tube local buckling zone, due to a better confinement to concrete core from outer steel SHS. Fig. 4(b1) displays overall failure modes of the beam specimens. A penetration crack (marked by a dashed circle) nearly extending to half-height of the section appears on the lower part of tube section, and meanwhile the primary local buckling (denotated by an arrow) occurs on the tube upper flange and portion of tube sidewalls relative to the penetration crack. This can be explained that, after the primary local buckling under compression of tube upper flange and portion of sidewalls occur, the neutral axis moves to the upper zone due to the redistribution of internal forces, leading to the rapid increase of the tensile stress of the lower part of tube section. Simultaneously, there are also 1-2 secondary local buckling in the tube upper flange, which are generally symmetric with the primary local buckling about the mid-span.

Failure modes of concrete core in the stub column specimens are demonstrated in Fig. 5(a1). It can be observed that, serious crushing of the concrete core generally happens at the primary local buckling area of tube walls and corners, while at the secondary local buckling zone in the steel tube the concrete core is crushed slightly or has no evident destruction. Additionally, with the specimens having a larger B/t as reference, the integrity of crushed concrete of the specimens with a smaller B/t is better, as the steel SHS with a smaller B/t has a better constraint on its concrete core. The failure modes of concrete core in the beam specimens are exhibited in Fig. 5(b1). Generally, severe crushing of concrete core also occurs at the primary local buckling area of steel SHS, while concrete core is slightly crushed or not damaged at the secondary local buckling area of steel SHS. Meanwhile, there is a main penetration cracking with a depth of about 80-90% of the sectional height of the concrete core, which starts at the cracking site of steel SHS and develops towards the primary local buckling area of steel SHS. Besides one main crack in the tensile zone, there are also a number of uniformly distributed fine cracks with a depth of about 2/3 of the sectional height of the concrete core.

2.4.2. Load versus deformation curves of the specimens

The curves of relationship between load and deformation of the specimens are indicated in Fig. 6, where Δ and N are axial displacement and the corresponding axial compressive load of stub columns respectively, and δ_{ms} and M are mid-span deflection and the corresponding bending moment of beams, respectively. In Fig. 6(b), the initial cracking of the tube tensile flange is marked by the inverted triangle symbol. It can be seen from Figs. 6(a1-1), (a2-1) and (b-1) that, as the deformations (Δ and δ_{ms}) increase, the evolution of the corresponding loads (N and M) of the SSC filled steel SHS specimens is generally similar to that of their counterparts with the OC, i.e. the $N-\Delta$ curve of the composite stub columns includes initial approximate elastic stage, subsequent elastic-plastic stage, sharp decline stage after peak load reached, and final stable change stage of the residual load resistance, while the $M-\delta_{\mathrm{ms}}$ curve of the composite beams consists of the initial approximate elastic phase, the subsequent elastic-plastic phase, later hardening phase, and the rapid decline phase of the bending resistance after the initial cracking of the tube tensile flange. Overall, for the stub column specimens under the same width (B) and mass substitution rate of SSA (R_{c} and/or R_{f}) and similar steel yield strength (f_{y}), the smaller the B/t value, the higher the curve slope before peak load achieved and the smaller the decline rate during sharp decline stage after peak load reached, mainly due to a better confinement of the steel SHS to its concrete core.

Fig. 7 shows the typical vertical displacement (δ) distribution over effective span of beam specimens, in which, $m(=M/M_{\mathrm{ue}})$ is the bending moment ratio, and the method for determining M_{ue} will be described in the next section; x is the distance from the fixed lower support, and the solid and dashed lines represent the measured displacement distribution and the corresponding sinusoidal half-wave curve with the same mid-span displacement as the measured one. It can be observed that, regardless of the type of the concrete core and the m value, the displacement distribution is generally close to the sinusoidal half-wave curve. Generally, while m greater than 0.9, the beam specimens with the SSC have smaller displacement than that with the OC. This may be due to the fact that, compared with the relevant OC, better friction between aggregates and hydration products caused by rougher surface of SSAs delays the tensile cracking of the SSC, leading to larger compression area of the concrete core in the later phase of loading.

2.4.3. Relationship between load and strain of outer steel tube

Fig. 8 shows the load (N and M) versus strain (ε) curves of outer steel SHS in the specimens. In Fig. 8(a), ε_{y} is yield strain of steel obtained based on the standard tensile coupon tests, and ε is the average value of all the symmetrical measuring points. In Fig. 8(b), ε_{L} is the average longitudinal strain. It can be seen from Figs. 8(a1-1)~(a4-1) that, on the whole, the $N-\varepsilon$ curves show a similar tendency to the $N-\Delta$ curves irrespective of $R_{\mathrm{c}}(R_{\mathrm{f}})$ and B/t; however, there is obvious difference in the post-peak stage of the $N-\varepsilon$ curves, which is mainly due to the evident discrepancy in the position and amount of tube local buckling caused by the existence of the randomly distributed material flaws. In addition, while reaching the peak load, all measured longitudinal strains at both side middle and corner are greater than ε_{y}, indicating that the properties of steel tube have been fully utilized, and the recorded peak load can be defined as the axial capacity (N_{ue}). It is shown in Fig. 8(b-1) that, irrespective of the type of concrete core and tube flange, all composite specimens generally have the $M-\varepsilon_{\mathrm{L}}$ curves of similar development trend. Furthermore, due to the concrete cracking and the damage of the interface between cracked concrete and steel tube, the $M-\varepsilon_{\mathrm{L}}$ curves fluctuate in the later stage. Similar to previous studies [21, 22], the flexural capacity ($M_{\mathrm{u,e}}$) is defined as the bending moment when ε_{L} of tube tension flange reaches 0.01. The measured axial capacity ($N_{\mathrm{u,e}}$) and flexural capacity ($M_{\mathrm{u,e}}$) are given in Table 2 and Table 3, respectively.

Until axial capacity is reached, the strain distribution of outer steel SHS at mid-height section of typical stub column specimens is indicated in Fig. 9, where y is distance from the symmetric axis, and $n(=N/N_{\mathrm{ue}})$ is axial load level. It can be found that, regardless of $R_{\mathrm{c}}(R_{\mathrm{f}})$ and B/t, the strain distribution generally exhibits similar characteristics. While $n \leq 0.6$, both the longitudinal and transverse strains increase almost proportionally, and the strains in the corner are close to those in the side middle; however, when $n > 0.6$, the increase amplitude of strains improves with the growth of n, and under the same n value, the longitudinal strain at the side middle is lower than that at the corner, while the transverse strain at the side middle is slightly higher than that at the corner. This can be explained that, the internal force redistribution occurs after the tube walls buckled locally, resulting in more axial load (that is, higher longitudinal strain) acting on the corner of the steel SHS, meanwhile, at the local buckling area of tube walls crushing and volume expansion of concrete core occur, and thus the coaction between steel SHS and concrete core causes higher transverse deformation of the tube walls. Additionally, the strains at each measuring point vary with the change of $R_{\mathrm{c}}(R_{\mathrm{f}})$ and B/t; however, the variation of strains is relatively limited when $n \leq 0.8$.

Fig. 10 shows the longitudinal strain distribution of outer steel SHS at mid-span section of typical beam specimens, where z is distance from the half-height of the section. It can be observed that, the longitudinal strain distribution along the section height basically conforms to the plane-section assumption when $n \leq 0.8$; however, while $n > 0.8$, on account of the aggravation of the local buckling of tube upper flange under compression, the tensile stress is concentrated to the tube lower flange opposite to the compressive local buckling area, so that tube lower flange with strain gauges (i.e. mid-span section) is unloaded, indicating that the longitudinal strain distribution along the section height is no longer consistent with the plane-section assumption. Moreover, with the increase of m, the centroid axis of the section gradually moves towards the compression zone, and the influence of $R_{\mathrm{c}}(R_{\mathrm{f}})$ on the longitudinal strain distribution characteristics is not obvious.

2.4.4. Mechanical indicators to measure the behaviour of the specimens

To discover the difference in the capacity between the SSC filled steel SHS specimens and the corresponding specimens with the OC, the axial capacity factor (F_{n}) and the flexural capacity factor (F_{m}) are defined as follows:

$$F_{\mathrm{n}} = \frac{N_{\mathrm{u,e-ssc}}}{N_{\mathrm{u,e-oc}}} \tag{1}$$

$$F_{\mathrm{m}} = \frac{M_{\mathrm{u,e-ssc}}}{M_{\mathrm{u,e-oc}}} \tag{2}$$

where, $N_{\mathrm{u,e-ssc}}(M_{\mathrm{u,e-ssc}})$ and $N_{\mathrm{u,e-oc}}(M_{\mathrm{u,e-oc}})$ are the measured axial (flexural) capacity of composite members containing the SSC and the corresponding composite member containing the OC, respectively. The obtained F_{n} and F_{m} are given in Table 2 and Table 3, respectively.

Comparison of the capacity ($N_{\mathrm{u,e}}$ and $M_{\mathrm{u,e}}$) and the corresponding capacity factor (F_{n} and F_{m}) of different specimens is shown in Fig. 11. It can be observed from Fig. 11(a) and Table 2 that, generally, under the same B/t value the SSC filled steel SHS stub column specimens possess a higher $N_{\mathrm{u,e}}$ than the corresponding specimen with the OC, and $N_{\mathrm{u,e}}$ changes similarly to f_{cu} as $R_{\mathrm{c}}(R_{\mathrm{f}})$ changes. When B/t=45.5, F_{n} varies between 0.963 and 1.088, and while B/t=32.6, F_{n} varies between 0.947 to 1.182. Under the same $R_{\mathrm{c}}(R_{\mathrm{f}})$ value, the composite specimens with a smaller B/t have a higher $N_{\mathrm{u,e}}$ as the steel SHS provides a better confinement to its concrete core. On average, $N_{\mathrm{u,e}}$ of the composite specimens with B/t=32.6 is 1.26 times those with B/t=45.5. Furthermore, within the range of $R_{\mathrm{c}}(R_{\mathrm{f}})$ considered in this study, the B/t value has no evident impact on the variation law of F_{n}. It can be found from Fig. 11(b) and Table 3 that, except for the beam specimen with R_{c} of 50%, $M_{\mathrm{u,e}}$ and F_{m} of the SSC filled steel SHS beams are very close to those of the corresponding beam with the OC. This is mainly because, when $M_{\mathrm{u,e}}$ is achieved the concrete in the tensile zone is unable to participate in bearing loads, and only the compressed concrete covering a small cross-section is involved in the moment bearing; however, its contribution to the flexural capacity is significantly lower than the outer tube [23]. As a result, compared with the OC and the beam specimen with the OC, the improvement in compressive strength of the SSC is not reflected in the flexural capacity of the SSC filled steel SHS beam specimens.

To evaluate the ability to resist deformation, the axial compressive stiffness $K_{\mathrm{s}}(=0.4N_{\mathrm{u,e}}/\varepsilon_{\mathrm{L,0.4}})$ of stub column specimens and the flexural stiffness $K_{\mathrm{b}}(=0.2\,M_{\mathrm{u,e}}/\phi_{0.2})$ of beam specimens are defined by referring to the methods in [24] and [21], respectively, in which $\varepsilon_{\mathrm{L,0.4}}$ is average longitudinal strain while reaching $0.4N_{\mathrm{u,e}}$ on the rising segment of the $N-\varepsilon_{\mathrm{L}}$ curve, and $\phi_{0.2}$ is curvature corresponding to $0.2M_{\mathrm{u,e}}$ on the rising segment of the $M-\phi$ curve, which is obtained based on the assumption that the vertical displacements conform to the sinusoidal half-wave curve.

The obtained K_s and K_b are listed in Table 2 and Table 3, respectively. At the same time, to quantitatively analyse the difference between the measured stiffness and the calculated one based on the superposition principle [22, 25], the axial compressive stiffness ratio (R_ks) and the flexural stiffness ratio (R_kb) are defined as follows:

$$R_\mathrm{ks} = \frac{K_\mathrm{s}}{E_\mathrm{s}A_s+E_\mathrm{c}A_\mathrm{c}} \tag{3}$$

$$R_\mathrm{kb} = \frac{K_\mathrm{b}}{E_\mathrm{s}I_s+0.2E_\mathrm{c}I_\mathrm{c}} \tag{4}$$

where, $A_\mathrm{s}(A_\mathrm{c})$ is cross-sectional area of outer steel SHS (concrete core), and $I_\mathrm{s}(I_c)$ is cross-sectional moment of inertia of outer steel SHS (concrete core). The values of R_ks and R_kb are also listed in Table 2 and Table 3, respectively.

Fig. 12 shows the variation in the stiffness (K_s and K_b) and the corresponding stiffness ratio (R_ks and R_kb) of the specimens. It can be found from Table 2 and Fig. 12(a) that, in general, K_s of the SSC filled steel SHS stub columns is higher than that of the corresponding composite stub columns with the OC, and the composite stub columns with a lower B/t have a higher K_s owing to a larger steel tube area under the same width. Additionally, R_ks varies between 0.982 and 1.110, and its mean value and standard deviation are 1.050 and 0.048, respectively, indicating that a satisfactory accurate prediction of the axial compressive stiffness of the SSC filled steel SHS stub columns can be obtained based on the direct superposition of the compressive stiffness of steel tube and concrete core. It is shown in Table 3 and Fig. 12(b) that, compared with the corresponding composite beam with the OC, there is a certain decrease in K_b of the SSC filled steel SHS beams. Simultaneously, R_kb changes between 0.872 and 1.013, and its mean value and standard deviation are 0.939 and 0.061, respectively, meaning that the superposition method based on ACI 318-19 [25] can give a relatively safe prediction for the flexural stiffness of the SSC filled steel SHS beams.

3. Numerical simulation

3.1. Finite element (FE) models

To numerically simulate the static responses of the SSC filled steel SHS stub columns and beams, nonlinear finite element (FE) models were established based on the general-purpose software

ABAQUS [26].

The property of steel tube in the SSC filled steel SHS members was simulated using the elastoplastic model in the ABAQUS [26]. For both the strengthened corner area and the un-strengthened flat area in cold-formed steel SHS, the Poisson's ratio and modulus of elasticity in the elastic stage were taken from the results of the tensile coupon tests (see Table 7), and the true stress-plastic strain relationship of steel in the plastic stage was transformed from engineering stress (σ_{s})-strain (ε_{s}) relationship suggested in [27] with the effect of the strain hardening of steel tube considered, as indicated in Eq. (5). Moreover, the radius (r) of the strengthened corner area was determined according to the method in [28], that is, when t<3.0 mm, r=2.0t, and when t ≥3.0 mm, r=2.5t. For the simplicity of modelling and acceleration of convergence, both endplates of the SSC filled steel SHS members were assumed to be an elastic material [22, 24].

$$\sigma_{\mathrm{s}}=\begin{cases}E_{\mathrm{s}}\varepsilon_{\mathrm{s}} & (\varepsilon_{\mathrm{s}}\le\varepsilon_1)\\ 0.75f_{\mathrm{y}}+0.5E_{\mathrm{s}}(\varepsilon_{\mathrm{s}}-\varepsilon_1) & (\varepsilon_1<\varepsilon_{\mathrm{s}}\le\varepsilon_2)\\ 0.875f_{\mathrm{y}}+0.1E_{\mathrm{s}}(\varepsilon_{\mathrm{s}}-\varepsilon_2) & (\varepsilon_2<\varepsilon_{\mathrm{s}}\le\varepsilon_3)\\ f_{\mathrm{y}}+0.005E_{\mathrm{s}}(\varepsilon_{\mathrm{s}}-\varepsilon_3) & (\varepsilon_{\mathrm{s}}>\varepsilon_3)\end{cases} \tag{5}$$

where, E_{s} is elastic modulus, $\varepsilon_1=0.75f_{\mathrm{y}}/E_{\mathrm{s}}$, $\varepsilon_2=f_{\mathrm{y}}/E_{\mathrm{s}}$, and $\varepsilon_3=2.25f_{\mathrm{y}}/E_{\mathrm{s}}$.

The property of concrete core in the SSC filled steel SHS members was simulated using damage plasticity model [26]. Regardless of the type of concrete core, E_{c} and Poisson's ratio of concrete (μ_{c}) in the elastic stage were respectively taken as $4730\sqrt{f_{\mathrm{c}}'}$ [25] and 0.2 [29], in which f_{c}' is cylindrical compressive strength. The research [30-35] showed that, reasonable reproduce of the properties of confined concrete after formation of splitting cracks is important for the simulation on the behaviour of composite members. However, the cracking criterion based on fracture energy [26] is temporarily adopted for reproducing the tensile property of concrete core after tensile cracking, as the actual measurement has not been carried out. The cracking stress of concrete under tension was set at $0.1f_{\mathrm{c}}'$. Furthermore, the data pairs of inelastic strain and compressive stress of concrete in the plastic stage was acquired based on the engineering stress (σ_{c})-strain (ε_{c}) model.

The limited studies on the constitutive ($\sigma_{\mathrm{c}}-\varepsilon_{\mathrm{c}}$) model of the SSC under compression [36-39] indicated that, compared with the relevant OC, the modulus of elasticity, peak stress and peak strain of the SSC were increased, and the increasing amplitude was mainly related to the mass substitution rate of SSA. Simultaneously, the peak stress of the engineering $\sigma_c - \varepsilon_c$ model of concrete is usually connected with the compressive strength. The tests on plain concrete specimens, including prisms, cylinders and cubes, had been carried out by many scholars to investigate the mechanical property of the SSC as well as the relationship between compressive strength of the SSC and that of the relevant OC, and the findings showed that, the effect of the mass substitution rate of SSA on the compressive strength of different block types of the SSC specimens was similar. As a result, to obtain sufficient samples, the block type of concrete specimens used in the strength tests was no longer distinguished when exploring the strength relationship between the SSC and the relevant OC. The compressive strength index ($K_{c,s}$) is defined as follows to weigh the effect of the mass substitution rate of SSA:

$$K_{c,s} = \frac{F_{ssc}}{F_{oc}} \tag{6}$$

where, F_{ssc} and F_{oc} are compressive strength of the SSC and the relevant OC, respectively.

Integriting the test information and consistency of test conditions, 218 effective test data were collected in this study, and the influence of the mass substitution rate of SSA on $K_{c,s}$ is shown in Fig. 13, where, R is the nominal mass substitution rate of SSA, for the SSC containing only one type of SSA, R is equal to the corresponding mass substitution rate of SSA, while for the SSC containing two types of SSA, R equals to the average value of the two mass substitution rate of SSA. It can be observed that, generally, $K_{c,s}$ has a tendency to increase and then decrease as R increases, and $K_{c,s}$ varies between 0.784 and 1.465 with an average value of 1.064, indicating that the compressive strength of the SSC is generally higher than that of the relevant OC.

Based on the regression analysis of the data in Fig 13, the data fitted formulae of $K_{c,s}$ can be obtained as follows:

$$K_{c,s} = \begin{cases} 0.4R + 1.0 & (R < 0.3) \\ -0.15R + 1.165 & (0.3 \le R \le 1.0) \end{cases} \tag{7}$$

According to the definition of $K_{c,s}$ and Eq. (7), the numerical relationship between the compressive strength of the SSC (F_{ssc}) and the relevant OC (F_{oc}) can be built. The comparison between the predicted ($F_{\mathrm{ssc,p}}$) and measured ($F_{\mathrm{ssc,m}}$) compressive strength of the SSC is displayed in Fig. 14, and the mean value and standard deviation of $F_{\mathrm{ssc,p}}/F_{\mathrm{ssc,m}}$ equal to 1.013 and 0.110, respectively, indicating that generally accurate prediction of the compressive strength of the SSC can be obtained based on the formulae in this study.

Given that the static performance of the SSC filled steel tubular members is similar to that of the reference CFST members, the compressive $\sigma_{\mathrm{c}} - \varepsilon_{\mathrm{c}}$ model of the filled SSC in the steel tube can be acquired by referring to the widely recognized one of the concrete core in the CFST [40]. As a result, the confinement factor (ξ_{ssc}) of the SSC filled steel tube is defined to reasonably consider the coaction between steel tube and its core SSC, and the formula for ξ_{ssc} is as follows:

$$\xi_{\mathrm{ssc}} = \frac{A_{\mathrm{s}} \cdot f_{\mathrm{y}}}{A_{\mathrm{c}} \cdot f_{\mathrm{ssck}}} \tag{8}$$

where, f_{ssck} is characteristic compressive strength of the SSC obtained by $K_{\mathrm{c,s}} \cdot f_{\mathrm{ock}}$, and f_{ock} is characteristic compressive strength of the relevant OC [40].

The results in Table 6 show that the measured strength of the five types of concrete is different, including both normal- and high-strength. The latest research [41-43] has revealed that, compared to normal-strength concrete lag between the development of axial strain and that of confining strain and stress exists for high-strength concrete due to its higher stiffness and less extensive development of cracks, that is, the confining stress of concrete in steel tube is affected by the stress-path dependence of confinement, which determines the constitutive model of confined concrete [34, 35, 43]. However, to simplify the model, this phenomenon is not considered in this study. Refer to the model in [40], the modified compressive $\sigma_{\mathrm{c}} - \varepsilon_{\mathrm{c}}$ model of the SSC can be expressed as follows:

$$y = \begin{cases} 2x - x^2 & (x \leq 1) \\ \dfrac{x}{\beta_0 \cdot (x-1)^{\eta} + x} & (x > 1) \end{cases} \tag{9}$$

where, $y = \sigma_{\mathrm{c}}/f'_{\mathrm{ssc}}$, $f'_{\mathrm{ssc}} = K_{\mathrm{c,s}} \cdot f'_{\mathrm{oc}}$; $x = \varepsilon_{\mathrm{c}}/\varepsilon_{\mathrm{c,p}}$; $\varepsilon_{\mathrm{c,p}} = (1300 + 12.5 f'_{\mathrm{ssc}} + 800\xi_{\mathrm{ssc}}^{0.2}) \cdot 1.0\mathrm{E}-6$; for circular section, $\beta_0 = 1.25\sqrt{f'_{\mathrm{ssc}}} \cdot (2.36\mathrm{E}-5)^{[0.25+(\xi_{\mathrm{ssc}}-0.5)^7]} \geq 0.12$ and $\eta = 2.0$, and for square section, $\beta_0 = 2.3(f'_{\mathrm{ssc}})^{0.1}/[1.2(1.0+\xi_{\mathrm{ssc}})^{0.5}]$ and $\eta = 1.6 + 1.5/x$; and f'_{ssc} and f'_{oc} are the cylindrical compressive strength of the SSC and the relevant OC, respectively. However, it should be noted that, for concrete core of similar compressive strength with various compositions of powder, the development of micro-cracks under compression will not be identical due to the difference in void content and wet packing density [44, 45], which may lead to different behaviours of concrete [46, 47].

It should be noted that, for the various compressive strength of the SSC, the measured value from test is used when test results are available, while Eqs. (6) and (7) are used to calculate the compressive strength of the SSC according to the design strength grade of the relevant OC if there are no test results. Moreover, when ξ_{ssc} equals to 0, Eq. (9) is also applicable to determine the stress-strain model of plain SSC under compression. The predicted typical stress-strain curves of the SSC under compression are compared with the measured results in Fig. 15. It can be found that, on the whole, the simulated curves match well with the measured ones.

The plasticity parameters for damage plasticity model of concrete took into account the suggested values of the software [26] and were individually calibrated by the existing test results, and the final consistent values adopted in the FE model were: dilation angle=30$^{\mathrm{o}}$, eccentricity of flow potential=0.1, ratio of initial equi-biaxial compressive yield stress to initial uniaxial compressive yield stress=1.16, ratio of the second stress invariant on tensile meridian to that on compressive meridian=2/3, and viscosity parameter=0. In addition, the damage factors were obtained by the method in [48].

The outer steel SHS was replicated using the shell elements (S4), and the modelling of core SSC and both endplates together with stiffeners (if any) was implemented using the solid elements (C3D8R). To guarantee the continuity and efficiency of computation, the same meshing nodes were arranged on steel SHS and concrete core, and denser element divisions were set at the corner area of the composite cross-section. The bond between steel SHS and concrete core was reproduced by the surface-to-surface contacts, and the 'hard contact' in the normal direction and the 'Coulomb friction' model in the tangential directions were defined [22, 24]. The FE model with meshes is exhibited in Fig. 16.

The boundary conditions of the axially compressed SSC filled steel SHS stub columns are indicated in Fig. 16(a). The restriction of all degrees of freedom, indicated by the 'ENCASTRE' in ABAQUS

[26], was applied to the bottom endplate, and the restriction of translational displacements in 2 horizontal directions (i.e. $U_X=U_Y=0$) was imposed on the top endplate. The loading was realized by applying an axial displacement to the top endplate until the axial displacement was greater than the experimentally measured value. The boundary conditions of the SSC filled steel SHS beams are displayed in Fig. 16(b). Same as the boundary conditions of the beam specimens in Fig 3(b), the restriction of 3 translational and 2 rotational degrees of freedom (i.e. $U_X=U_Y=U_Z=0$ and $UR_Y=UR_Z=0$) was applied to the fixed hinge support, while the restriction of 2 translational and 2 rotational degrees of freedom (i.e. $U_X=U_Y=0$ and $UR_Y=UR_Z=0$) was imposed on the rolling hinge support. The loading was applied through a vertical displacement to the element nodes on the outer surface of tube upper flange located at two quartiles of the beam, and in order to ensure the accuracy of the loading position, a cutting surface was set at both quartiles before conducting element division. The loading stopped when the mid-span deflection was larger than that recorded in the experiments. In addition, according to the research outcomes in [49], the initial flaws and residual stresses in the steel SHSs were not considered while conducting the FE simulation on the static performance of the SSC filled steel SHS members.

3.2. Validation of the FE models

FE simulation results show that, similar to the test results, the mass substitution rate of SSA (R_c and/or R_f) has a very limited impact on the failure modes and the trend of load-deformation curves, but has certain effect on the mechanical indicators of the tested composite specimens in this study. The simulated failure modes of typical SSC filled steel SHS specimens are also demonstrated in Figs. 4 and 5, where the mode of the steel SHS is indicated by the Mises stress, and the mode of the concrete core is presented by the logarithmic strain in Z direction. It is shown in Figs. 4(a2) and (b2) that, as a whole, the modelled ring-shape primary local buckling of steel SHS in the stub columns, and overall deflection as well as primary local buckling of tube upper flange of the beams agree well with the observed results in the tests. However, the simulated position and number of the local buckling of the steel SHS have some difference from the measured results, i.e. the redistribution of forces/moment due to the formation of plastic hinges after some parts of the confinement are yielded/fractured or concrete crushed is not well captured, and there is no tube flange cracking in the tension area of the simulated beam models. These may be attributed to the processing deviation of steel tube, the faculative material flaws in the specimens and the extra eccentricity of the stub columns or out-of-plane deformation of the beams in the late loading period, which cannot be reasonably included in the FE model of this study. Furthermore, simplified simulation on the concrete after formation of splitting cracks is also the reason for the difference between simulated and measured results. It is demonstrated in Figs. 5(a2) and (b2) that, apart from the difference between the simulated and measured overall failure modes of the specimens, the modelled failure characteristics of concrete core are basically analogous to the measured ones, i.e. the concrete compressive strain of the stub columns and beams is the largest (crushing) at the position where the maximum local buckling deformation of steel SHS occurs, while the tensile strain of concrete core in the beams is the largest (cracking) within the range between the two quarters, having an approximately uniform distribution of tensile strains.

The simulated load (N) versus deformation (Δ and ε) curves of the SSC filled steel SHS stub columns as well as bending moment (M) versus deformation (δ_{ms} and ε) curves of the SSC filled steel SHS beams are compared with the measured curves in Figs. 6 and 8, respectively. It can be seen that, generally, the simulated evolution of loads as the deformations increase is similar to that of measurement; however, the simulated curves deviate from the measured results to some extent from the beginning of the tube local bucking until the test was terminated. This can be explained that, some conditions of the experiments, such as material flaws and geometric size deviations in the specimens, the difference in position and angle of measuring equipment from the planning results and randomness of compressive local buckling site of steel SHS, were difficult to be legitimately quantified in the present FE model.

The predicted capacity using the FE model ($N_{\mathrm{u,fe}}$ and $M_{\mathrm{u,fe}}$) together with the ratio of predicted capacity to measured capacity of the composite specimens in this study are presented in Tables 2 and 3. Fig. 17 demonstrates the change in the ratio of predicted capacity to measured capacity of the SSC filled steel SHS stub column and beam specimens with respect to R. It is shown that, the ratio is generally from 0.873 to 1.013, and the calculation results indicate that, the mean value and standard deviation of the ratio are 0.954 and 0.039, respectively. Generally, the predicted axial/flexural capacities of the SSC filled steel SHS member using the FE model agree well with the experimental results and are on the safe side. The reasons for the deviation of ratio of $N_{\mathrm{u,fe}}(M_{\mathrm{u,fe}})$ to $N_{\mathrm{u,e}}(M_{\mathrm{u,e}})$ from unity may lie in: 1) the difference in material properties between composite specimen and standard test-pieces (steel coupons and concrete blocks) exists, 2) the variation in R_{c} and/or R_{f} has influence on the behaviour of concrete, and 3) the actual sizes of steel tube in the composite specimen are different from the designed ones.

Based on the parameters in the tests, it can be found that the applicable range of the proposed model should be limited to: f'_{ssc}=35.3-61.8 MPa, f_{y}=305.8-398.9 MPa, B/t=32.6-46.0, B=120-180 mm, L/B=3.0 (stub column), R_{c}=0-100%, and/or R_{f}=0-50%. Furthermore, precise reproduce of concrete cracking in the FE modelling will be helpful to improve the prediction accuracy of the performance of the SSC filled steel SHS stub columns and beams.

4. Prediction of axial/flexural capacity

The experimental observations presented in this study and the existing literature [12] as well as the FE simulation results of this study show that, generally, the failure modes and the load versus deformation relationship of the SSC filled steel SHS stub columns and beams are similar to the corresponding composite members with the OC, and the difference in the capacity between them is mainly caused by the difference in the compressive strength of concrete core, that is, the difference in the mass substitution rate of SSA (R_{c} and/or R_{f}). Therefore, this study focuses on the applicability of the method in the existing technical standards of the CFST structures [23, 25, 50-52] for the prediction of the axial/flexural capacity of the SSC filled steel SHS members, and the measured properties of the steel SHS and the SSC were used. In order to compare under the same conditions, the partial coefficient of each material was set as unity while calculating the capacity of the SSC filled steel SHS members by the method in the design standards.

The comparison between the calculated and measured capacities of the SSC filled steel SHS specimen is presented in Table 8. It can be found that, for the SSC filled steel SHS stub columns, the predicted axial capacities using the above technical standards are generally lower than the measured results. The average of the predicted axial capacities using the formula of ACI 318-19, AIJ and ANSI/AISC 360-16 is about 15% lower than that of the measured results, and in general, EN 1994-1-1 and GB/T 51446-2021 give the best prediction as their predicted axial capacities are closer to the experimental results than those of the other three standards, although having a slightly higher standard deviation. For the SSC filled steel SHS beams, AIJ, ANSI/AISC 360-16, EN 1994-1-1 and GB/T 51446-2021 predict the flexural capacities about 23%, 23%, 10% and 12% lower than the experimental results respectively, and generally ACI 318-19 with mean value and standard deviation of 0.921 and 0.043 respectively gives the best prediction. The discrepancy between the calculated and measured capacities is caused by the following reasons: 1) the confinement of steel tube to concrete core is not considered in the formulae; 2) the contribution of concrete core to flexural capacity is not included; and 3) the formulae obtained from theoretical derivation or numerical regression always tend to be conservative.

5. Conclusions

The static performance of steel slag concrete (SSC) filled steel square hollow section (SHS) stub columns as well as beams is experimentally and numerically studied in this paper, and on the basis of the observations the main conclusions are as follows:

(1) The overall failure modes, the local failure mode of concrete core in the steel tube, the evolution of loads with the increase of the deformations, as well as the development process of the deformations of typical SSC filled steel SHS specimens are generally similar to those of the reference specimens with the OC. Moreover, the SSC filled steel SHS stub columns with a smaller B/t have a better axial compressive performance.

(2) The experimental results of the representative specimens show that, regardless of R_c and/or R_f, the capacity and stiffness of the SSC filled steel SHS stub columns under axial compression are greater than those of the reference specimens with the OC, and the flexural capacity of the former is similar to that of the latter; however, the flexural stiffness of the former is significantly lower than that of the latter. In general, the axial compressive/flexural stiffness of the SSC filled steel SHS members can be accurately predicted by the superposition method.

(3) Considering the effect of R_c and/or R_f on the compressive strength of the SSC, a modified engineering stress-strain model for the SSC under compression is proposed by this research, and generally the static performance of the SSC filled steel SHS stub columns and beams can be predicted well by the established finite element (FE) model including the modified constitutive model for the SSC mentioned above.

(4) Overall, axial capacity of the SSC filled steel SHS stub columns can be predicted safely and accurately by EN 1994-1-1 and GB/T 51446-2021, while ACI 318-19 is the best predictor for the flexural capacity of the SSC filled steel SHS beams.

Declaration of Competing Interest

The authors declare that they have no known competing financial interests or personal relationships that could have appeared to influence the work reported in this paper.

Acknowledgement:

The research work reported herein was supported by the National Natural Science Foundation of China (No. 51678105). The research funding is highly appreciated. The authors also wish to thank Mr. Ke Lai for his help in the tests.

References:

[1] A.M. Rashad, Behavior of steel slag aggregate in mortar and concrete-A comprehensive overview, J. Build. Eng. 53 (2022) 104536.

[2] O. Gencel, O. Karadag, O.H. Oren, T. Bilir, Steel slag and its applications in cement and concrete technology: A review, Construct. Build. Mater. 283 (2021) 122783.

[3] Q. Dong, G. Wang, X. Chen, J. Tan, X. Gu, Recycling of steel slag aggregate in portland cement concrete: An overview, Journal of Cleaner Production 282 (2021) 124447.

[4] J. Guo, Y. Bao, M. Wang, Steel slag in China: Treatment, recycling, and management, Waste Management 78 (2018) 318-330.

[5] B. Huo, B. Li, C. Chen, Y. Zhang, Surface etching and early age hydration mechanisms of steel slag powder with formic acid, Construct. Build. Mater. 280 (2021) 122500.

[6] GB/T 14685-2011, Pebble and Crushed Stone for Conctruction, China Standard Press, Beijing, China, 2011. (in Chinese)

[7] GB/T 14684-2011, Sand for Conctruction, China Standard Press, Beijing, China, 2011. (in Chinese)

[8] C33/C33M-13, Standard Specification for Concrete Aggregates, ASTM International, PA, USA, 2013.

[9] S. Saxena, A.R. Tembhurkar, Impact of use of steel slag as coarse aggregate and wastewater on fresh and hardened properties of concrete, Construct. Build. Mater. 165 (2018) 126-137.

[10] N.H. Roslan, M. Ismail, N.H.A. Khalid, B. Muhammad, Properties of concrete containing electric arc furnace steel slag and steel sludge, J. Build. Eng. 28 (2020) 101060.

[11] L.H. Han, Y.F. Yang, H. Yang, W. Li, Life-cycle based analytical theory of concrete-filled steel tubular structures and its applications, Chin. Sci. Bull. 65(28-29) (2020) 3173-3184.

[12] X. Yu, Z. Tao, T.Y. Song, Effect of different types of aggregates on the performance of concrete-filled steel tubular stub columns, Mater. Struct. 49(9) (2016) 3591-3605.

[13] F. Yu, Y. Fang, Y. Zhang, L. Xu, R. Bai, Mechanical behavior of self-stressing steel slag aggregate concrete filled steel tubular stub columns, Structural Concrete, 21(4) (2020) 1597-1611.

[14] Q.H. Wang, J.F. Liang, C.F. He, W. Li, Axial compressive behavior of lithium slag recycled coarse aggregate concrete-filled circular steel stub columns, Advances in Materials Science and Engineering 2022 (2022) 3658617.

[15] R.M. Abendeh, D. Salman, R. Al Louzi, Experimental and numerical investigations of interfacial bond in self-compacting concrete-filled steel tubes made with waste steel slag aggregates, Developments in the Built Environment 11 (2022) 100080.

[16] C. Luo, F. Wang, H. Chen, A. Qi, Y. Chen, Study on the hysteretic behavior of recycled aggregate concrete-filled steel tube columns containing ferronickel slag, J. Build. Eng. 46 (2022) 103695.

[17] P. Feng, Z. Li, S. Zhang, J.Q. Yang, Steel slag aggregate concrete filled-in FRP tubes: Volume expansion effect and axial compressive behaviour, Construct. Build. Mater. 318 (2022) 125961.

[18] M. Maslehuddin, A.M. Sharif, M. Shameem, M. Ibrahim, M.S. Barry, Comparison of properties of steel slag and crushed limestone aggregate concretes, Construct. Build. Mater. 17(2) (2003) 105-112.

[19] J.S. Lim, C.B. Cheah, M.B. Ramli, The setting behavior, mechanical properties and drying shrinkage of ternary blended concrete containing granite quarry dust and processed steel slag aggregate, Construct. Build. Mater. 215 (2019) 447–461.

[20] P. Singh, A.B. Danie Roy, H. Singh, Mechanical and durability properties of concrete incorporating weathered coarse Linz-Donawitz (LD) steel slag, J. Build. Eng. 61 (2022) 105301.

[21] L.H. Han, H. Lu, G.H. Yao, F.Y. Liao, Further study on the flexural behaviour of concrete-filled steel tubes, J. Constr. Steel Res. 62(6) (2006) 554-565.

[22] Y.F. Yang, Y.Q. Zhang, F. Fu, Performance and design of RAC-filled steel RHS beams, J. Build. Eng. 46 (2022) 103734.

[23] EN 1994-1-1, Eurocode 4: Design of Composite Steel and Concrete Structures-Part 1-1: General Rules and Rules for Buildings, European Committee for Standardization (CEN), Brussels, Belgium, 2004.

[24] Y.F. Yang, C. Hou, M. Liu, Tests and numerical simulation of rectangular RACFST stub columns under concentric compression, Structures 27 (2020) 396-410.

[25] ACI Committee 318, Building Code Requirements for Structural Concrete (ACI 318-19) and Commentary, American Concrete Institute, Detroit, USA, 2019.

[26] Simulia, ABAQUS 6.14 Analysis User's Manual, Dassault Systemes Simulia Corp., Providence, RI, USA, 2014.

[27] N. Abdel-Rahman, K.S. Sivakumaran, Material properties models for analysis of cold-formed

steel members, J. Struct. Eng. 123(9) (1997) 1135-1143.

[28] M. Elchalakani, X.L. Zhao, R. Grzebieta, Tests on concrete filled double-skin (CHS outer and SHS inner) composite short columns under axial compression, Thin-Walled Struct. 40(5) (2002) 415-441.

[29] FIB, Fib Model Code for Concrete Structures 2010, Fédération Internationale du Béton, Ernst & Sohn, Berlin, Germany, 2013.

[30] C.X. Dong, A.K.H. Kwan, J.C.M. Ho. A constitutive model for predicting the lateral strain of confined concrete. Engineering Structures 91 (2015) 155-166.

[31] A.K.H. Kwan, C.X. Dong, J.C.M. Ho. Axial and lateral stress–strain model for FRP confined concrete. Engineering Structures 99 (2015) 285-295.

[32] S.H. Lo, A.K.H. Kwan, Y. Ouyang, J.C.M. Ho. Finite element analysis of axially loaded FRP-confined rectangular concrete columns. Engineering Structures 100 (2015) 253-263.

[33] M. Lai, L. Hanzic, J.C.M. Ho. Fillers to improve passing ability of concrete. Structural Concrete 20(1) 2019 185-197.

[34] Y. Ouyang, A.K.H. Kwan. Finite element analysis of square concrete-filled steel tube (CFST) columns under axial compressive load. Engineering Structures 156 (2018) 443-459.

[35] Y. Ouyang, A.K.H. Kwan. Use of analytical lateral-axial strain relation in FE analysis of axially loaded rectangular CFST columns. Engineering Structures 166 (2018) 142-151.

[36] Y. Guo, J. Xie, J. Zhao, K. Zuo, Utilization of unprocessed steel slag as fine aggregate in normal- and high-strength concrete, Construct. Build. Mater. 204 (2019) 41–49.

[37] B. Li, Y. Li, C. Wang, F. Cao, Experimental study on stress-strain curve of granulated steel slag concrete, J. Build. Struct. 40(8) (2019) 163-169. (in Chinese)

[38] G. Xue, Y. Zhao, H. Zhou, L. Sun Experimental study on mechanical properties and constitutive relationship of steel slag aggregate reinforced concrete, Engineering Mechanics 39(5) (2022) 86-95. (in Chinese)

[39] G. Xue, Q. Fu, S. Xu, J. Li, Macroscopic mechanical properties and microstructure characteristics of steel slag fine aggregate concrete, J. Build. Eng. 56 (2022) 104742.

[40] L.H. Han, G.H. Yao, Z. Tao, Performance of concrete-filled thin-walled steel tubes under pure torsion, Thin-Walled Struct. 45(1) (2007) 24-36.

[41] M.H. Lai, Y.W. Liang, Q. Wang, F.M. Ren, M.T. Chen, J.C.M. Ho. A stress-path dependent stress-strain model for FRP-confined concrete. Engineering Structures 203 (2020) 109824.

[42] M.H. Lai, W. Song, X.L. Ou, M.T. Chen, Q. Wang, J.C.M. Ho. A path dependent stress-strain model for concrete-filled-steel-tube column. Engineering Structures 211 (2020) 110312.

[43] S. Lin, Y.G. Zhao, Z.H. Lu. Modified confining stress path dependent analytical model for axially loaded circular normal, high and ultra-high strength concrete-filled steel tube stub columns. Composite Structures 242 (2020) 112192.

[44] H.H.C. Wong, A.K.H. Kwan. Packing density of cementitious materials: part 1-measurement using a wet packing method. Materials and Structures, 41(4) (2008) 689-701.

[45] A.K.H. Kwan, H.H.C. Wong. Packing density of cementitious materials: part 2-packing and flow of OPC+PFA+CSF. Materials and Structures, 41(4) (2008) 773-784.

[46] A.K.H. Kwan, C.X. Dong, J.C.M. Ho. Axial and lateral stress–strain model for circular concrete-filled steel tubes with external steel confinement. Engineering Structures 117 (2016) 528-541.

[47] C.X. Dong, A.K.H. Kwan, J.C.M. Ho. Effects of external confinement on structural performance of concrete-filled steel tubes. Journal of Constructional Steel Research 132 (2017) 72-82.

[48] V. Birtel, P. Mark, Parameterised finite element modelling of RC beam shear failure, Proceedings of the 19th Annual International ABAQUS Users' Conference, Boston, USA, (2006) 95-108.

[49] Z. Tao, Z.B. Wang, Q. Yu, Finite element modelling of concrete-filled steel stub columns under axial compression, J. Constr. Steel Res. 89 (2013) 121-131.

[50] AIJ. Recommendations for Design and Construction of Concrete Filled Steel Tubular Structures, Architectural Institute of Japan, Tokyo, Japan, 2008.

[51] ANSI/AISC 360-16, Specification for Structural Steel Buildings, American Institute of Steel Construction, Chicago, USA, 2016.

[52] GB/T 51446-2021. Technical Standard for Concrete-Filled Steel Tubular Hybrid Structures. China Architecture & Building Press, Beijing, China, 2021.

Figures:

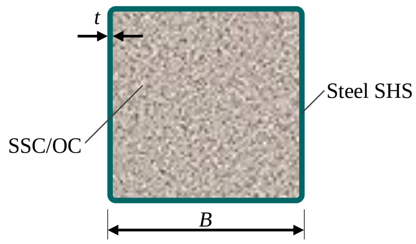

Fig. 1. Cross-section of the specimens.

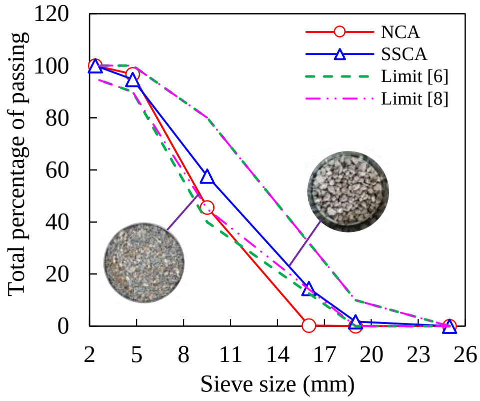

(a) Coarse aggregate

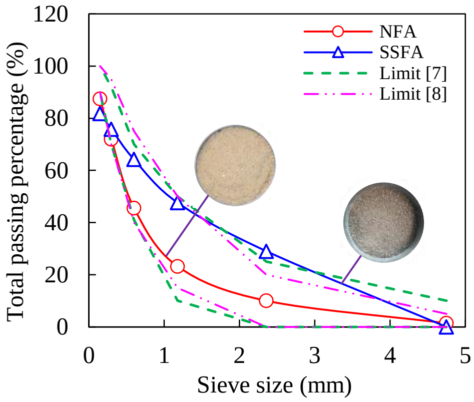

(b) Fine aggregate

Fig. 2. Grading of different kinds of aggregates.

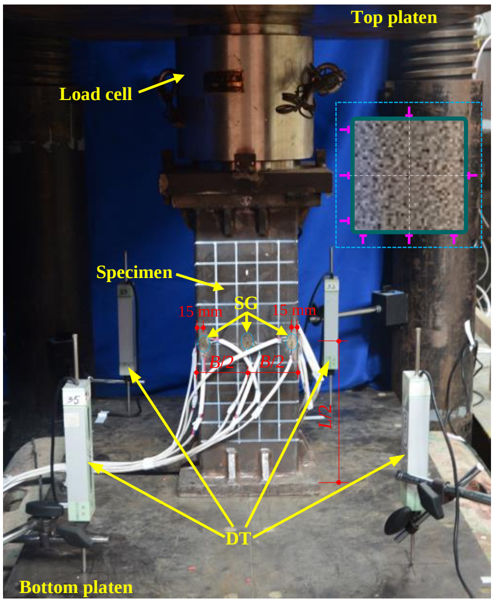

(a) Stub columns

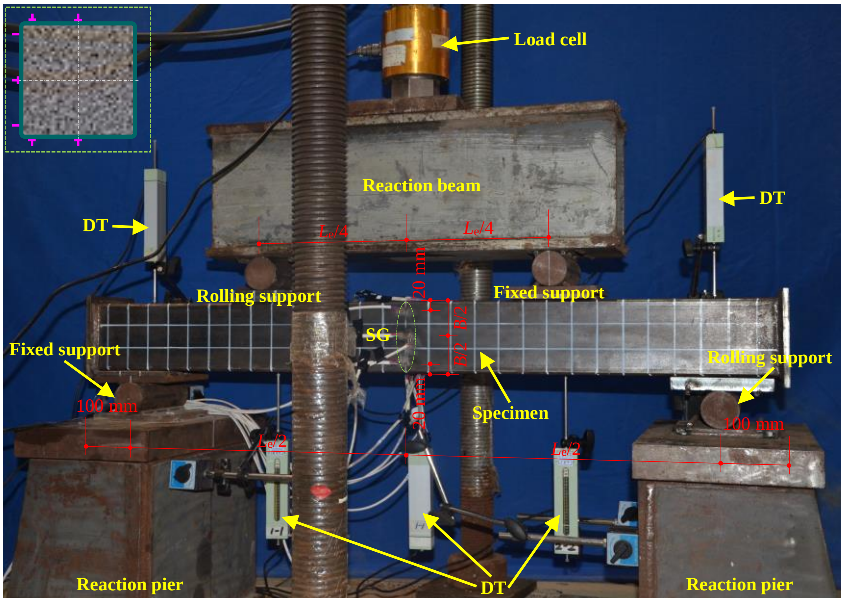

(b) Beams

Fig. 3. Picture of test set-up and measurement of the specimens.

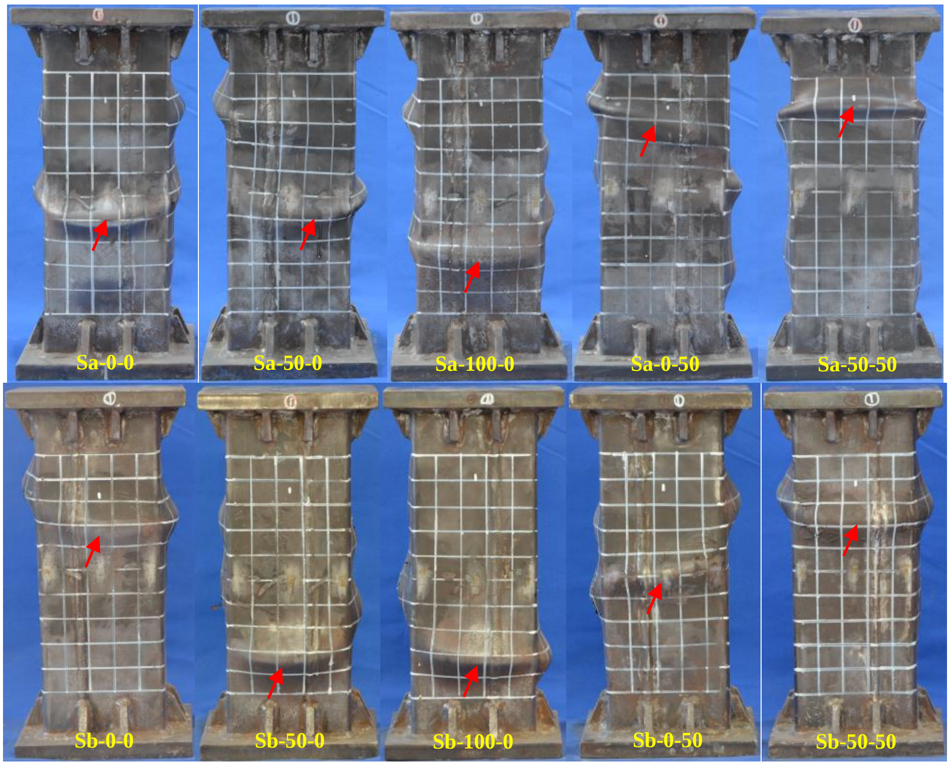

(1) Test results

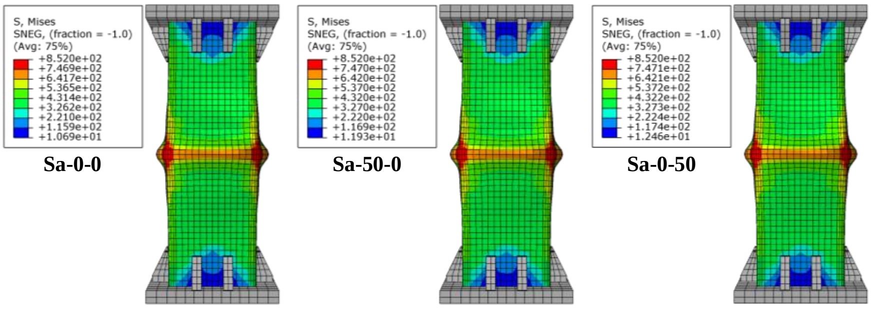

(2) Typical simulation results

(a) Stub columns

Fig. 4. (continued)

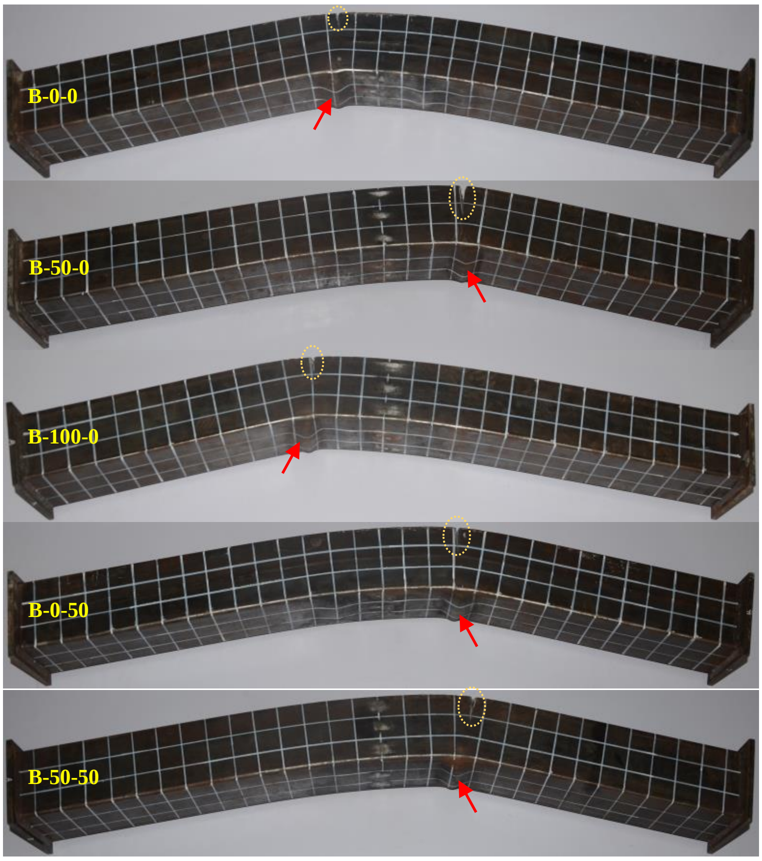

(1) Test results

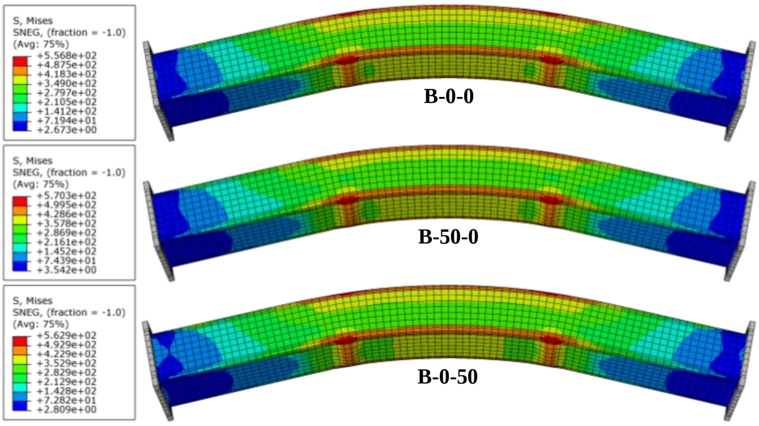

(2) Typical simulation results

(b) Beams

Fig. 4. Overall failure modes of the specimens.

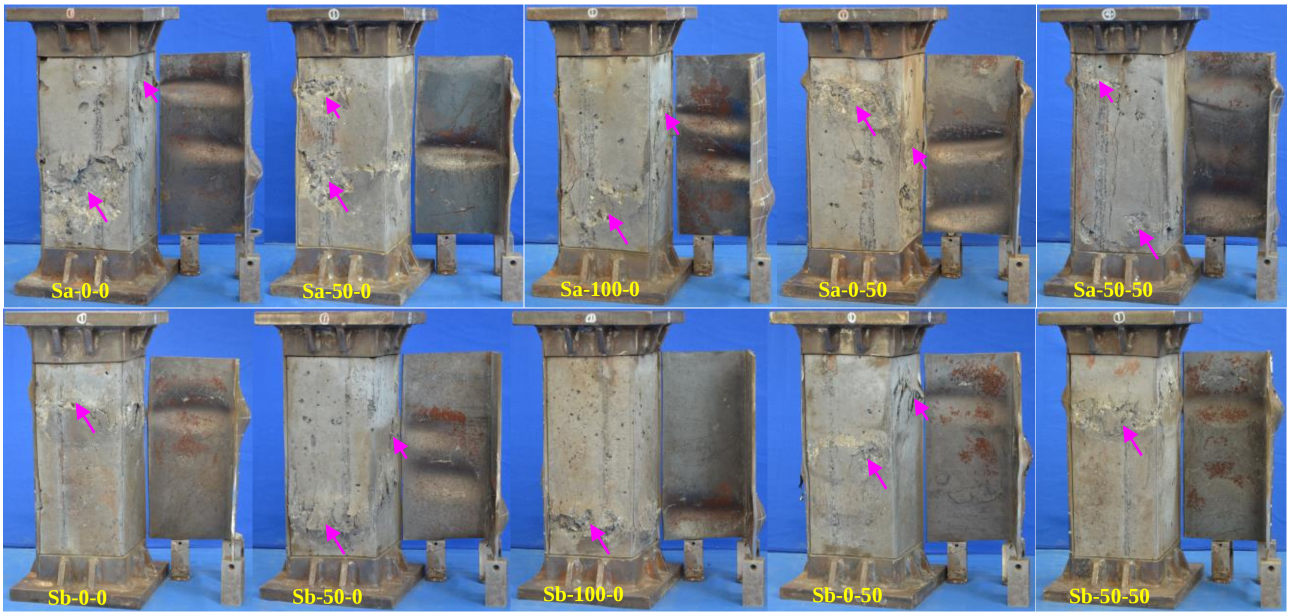

(1) Test results

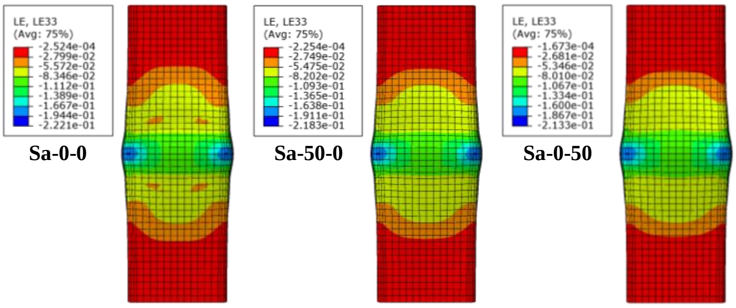

(2) Typical simulation results

(a) Stub columns

Fig. 5. (continued)

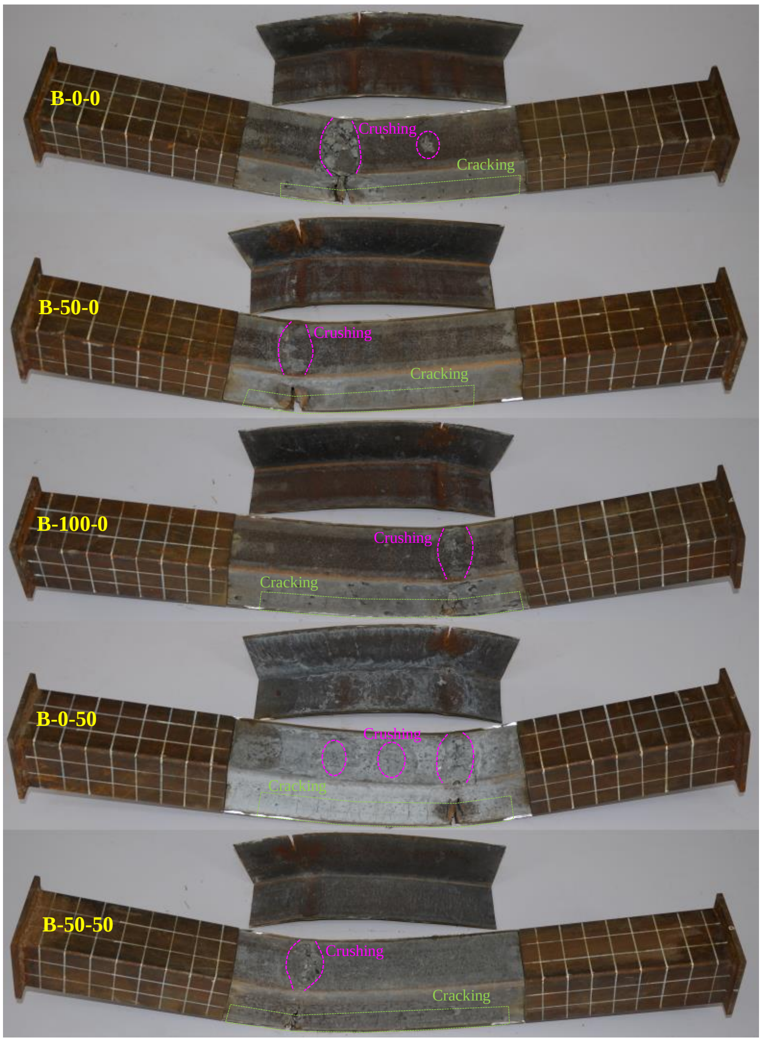

(1) Test results

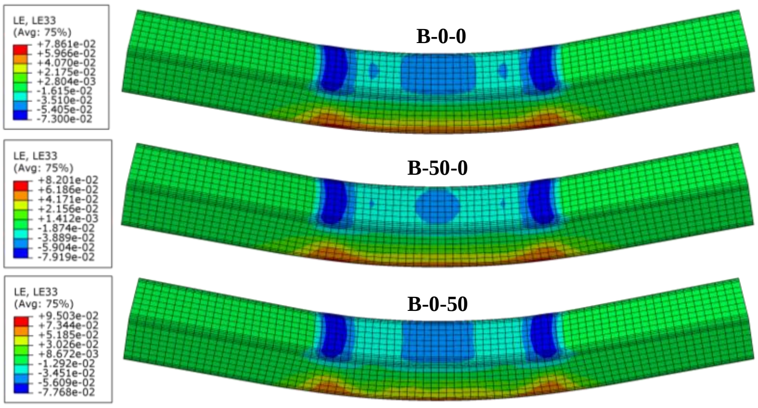

(2) Typical simulation results

(b) Beams

Fig. 5. Failure modes of core concrete in the specimens.

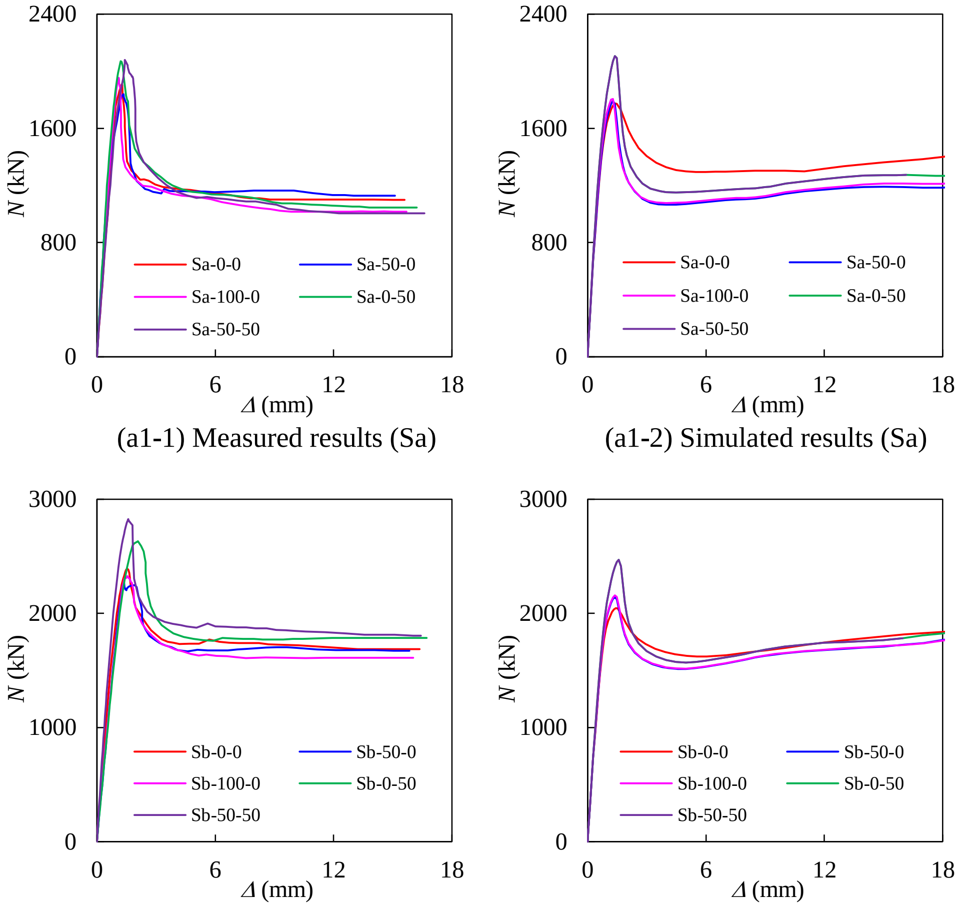

(a1-1) Measured results (Sa) (a1-2) Simulated results (Sa)

(a2-1) Measured results (Sb) (a2-2) Simulated results (Sb)

(a) $N-\Delta$ curve of the stub columns

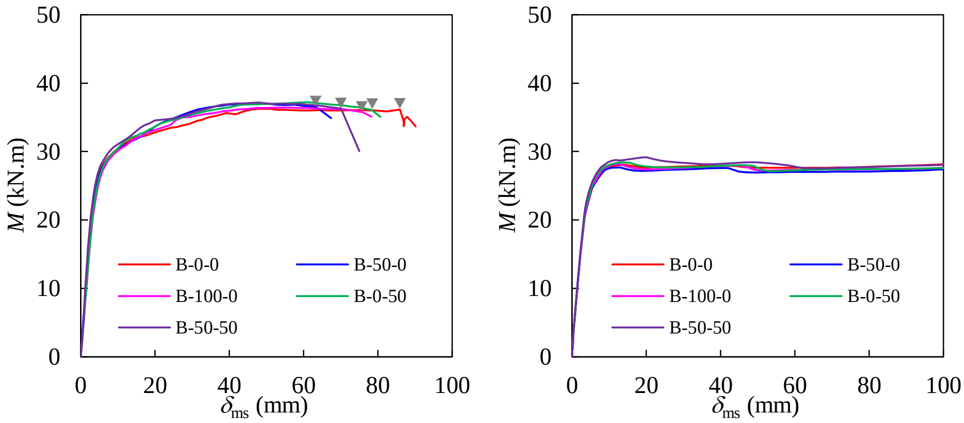

(b-1) Measured results (b-2) Simulated results

(b) $M-\delta_{\mathrm{ms}}$ curve of the beams

Fig. 6. Load versus deformation curve of the specimens.

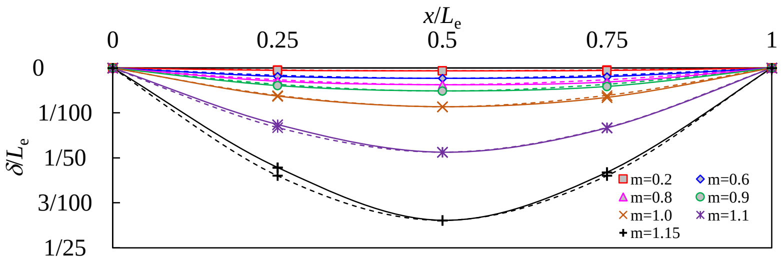

(a) B-0-0

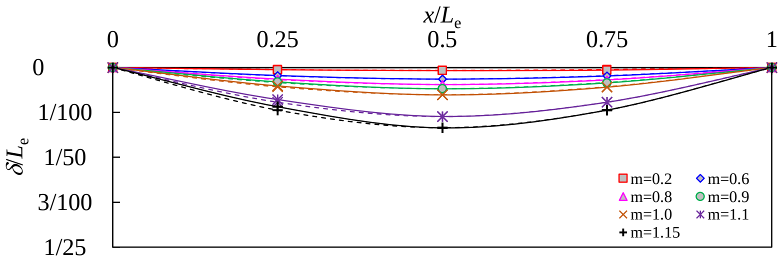

(b) B-100-0

Fig. 7. Typical vertical displacement distribution over effective span of beam specimens.

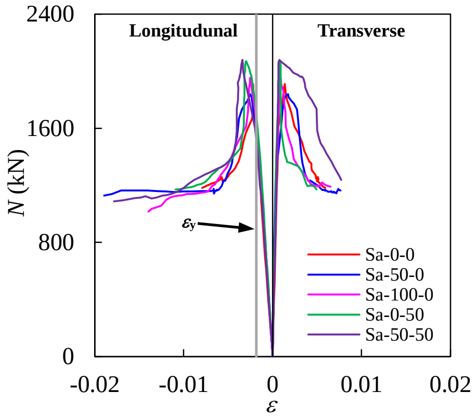

(a1-1) Measured results (Sa: side middle)

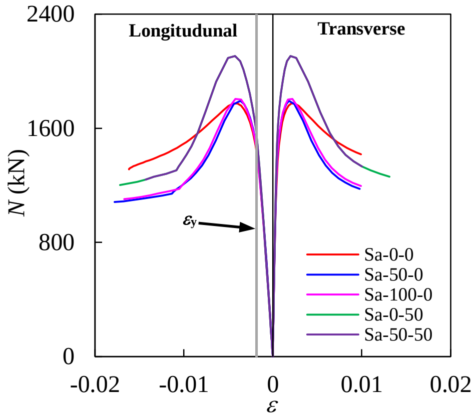

(a1-2) Simulated results (Sa: side middle)

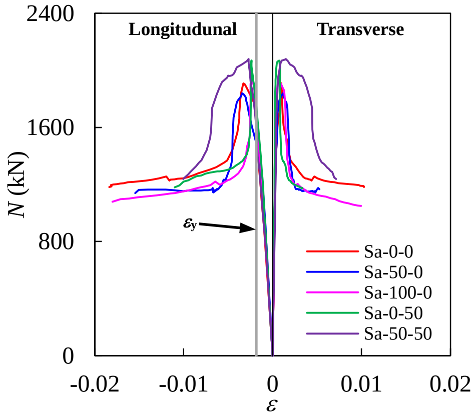

(a2-1) Measured results (Sa: corner)

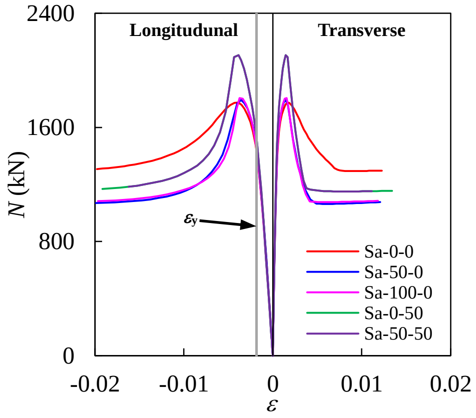

(a2-2) Simulated results (Sa: corner)

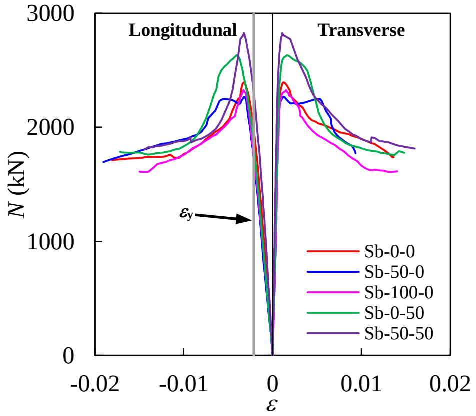

(a3-1) Measured results (Sb: side middle)

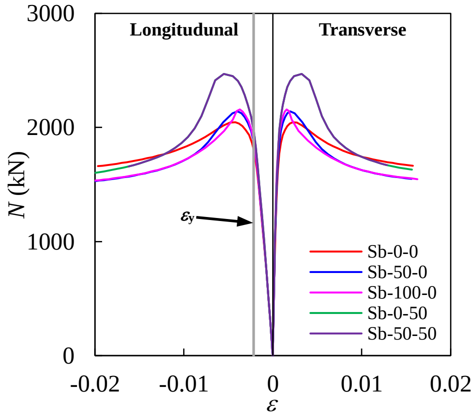

(a3-2) Simulated results (Sb: side middle)

Fig. 8. (continued)

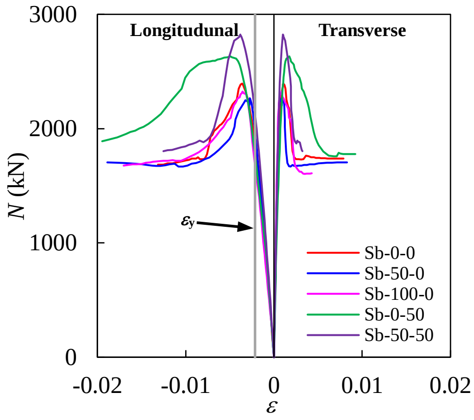

(a4-1) Measured results (Sb: corner)

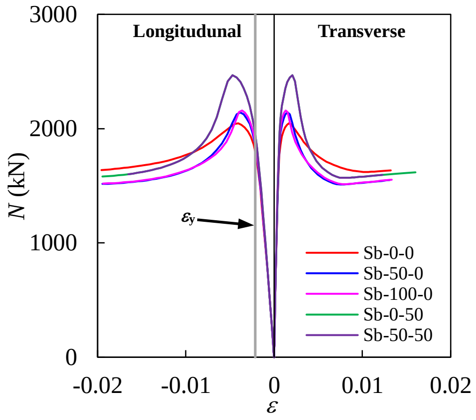

(a4-2) Simulated results (Sb: corner)

(a) $N-\varepsilon$ curve of the stub columns

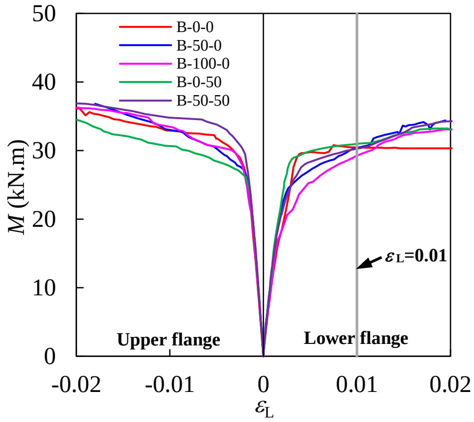

(b-1) Measured results

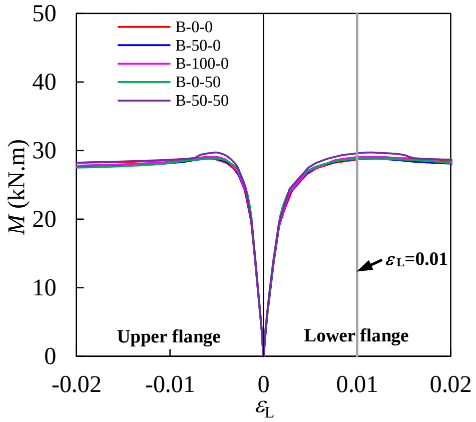

(b-2) Simulated results

(b) $M-\varepsilon_{\mathrm{L}}$ curve of the beams

Fig. 8. Load versus strain curves of outer steel SHS of the specimens.

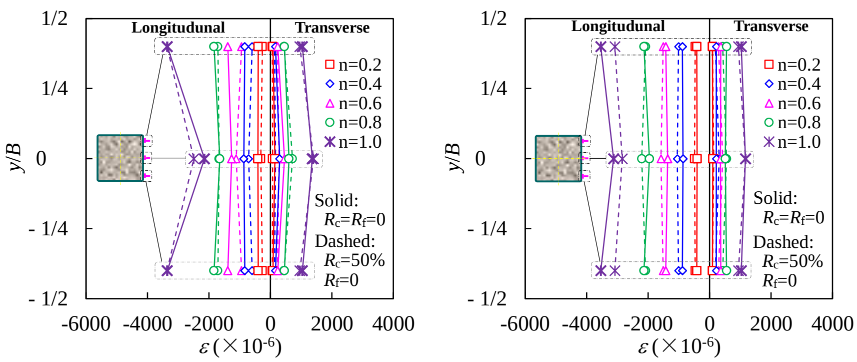

(a) Sa series (b) Sb series

Fig. 9. Strain distribution of outer steel SHS at mid-height section of typical stub column specimens.

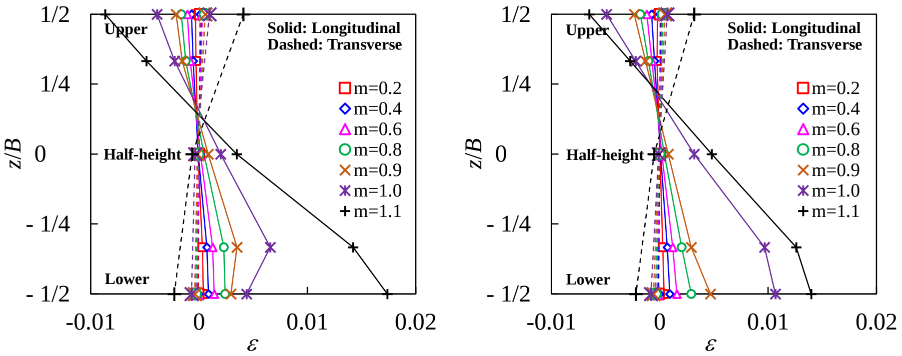

(a) B-0-0

(b) B-0-50

Fig. 10. Strain distribution of outer steel SHS at mid-span section of typical beam specimens.

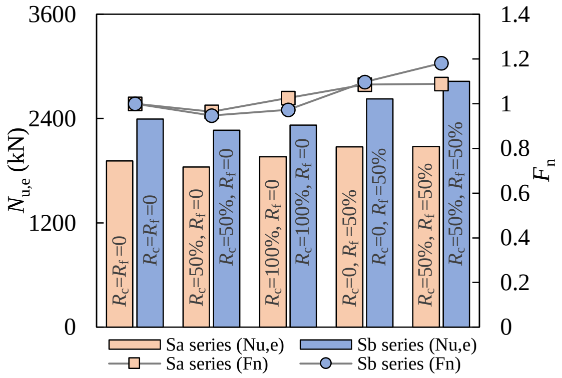

(a) $N_{u,e}$ and F_n of stub columns

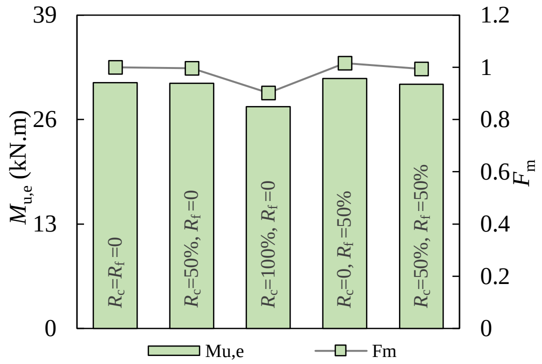

(b) $M_{u,e}$ and F_m of beams

Fig. 11. Comparison of the capacity and the corresponding capacity factor of different specimens.

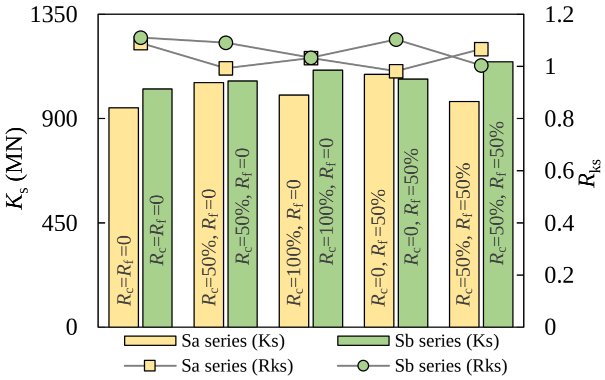

(a) K_s and R_{ks} of stub columns

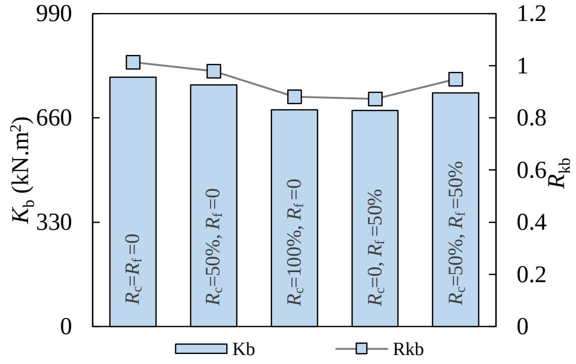

(b) K_b and R_{kb} of beams

Fig. 12. Variation in the stiffness and the corresponding stiffness ratio of the specimens.

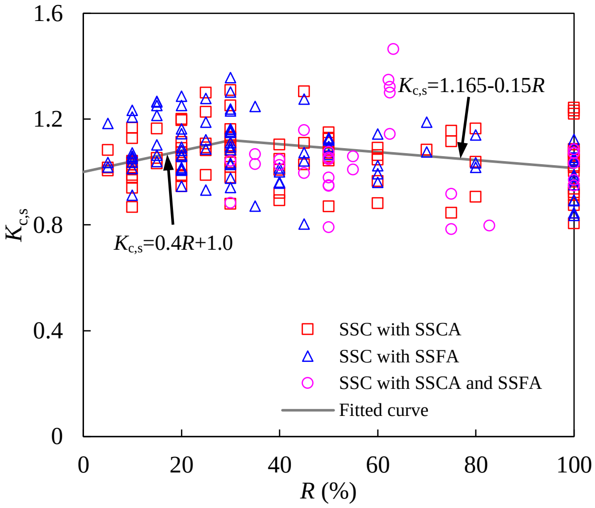

Fig. 13. Compressive strength index ($K_{c,s}$) of the SSC according to the experimental results.

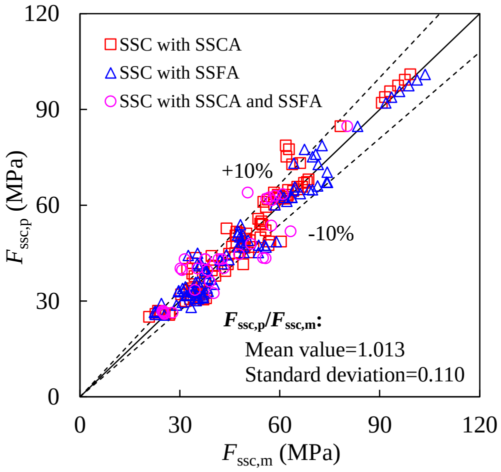

Fig. 14. Comparison between the predicted and measured compressive strength of the SSC.

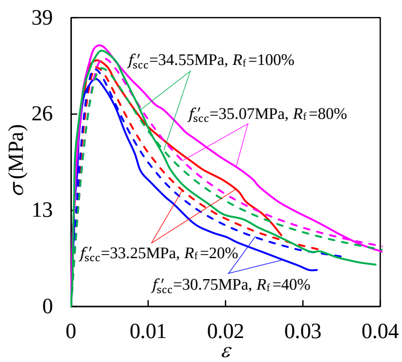

(a) Test of cylinders [37]

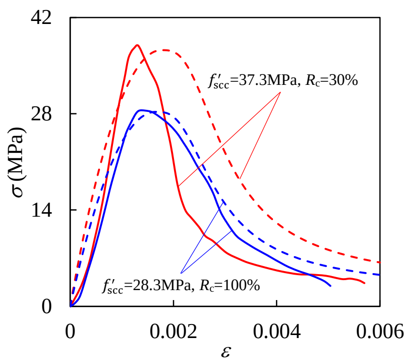

(c) Test of prisms [38]

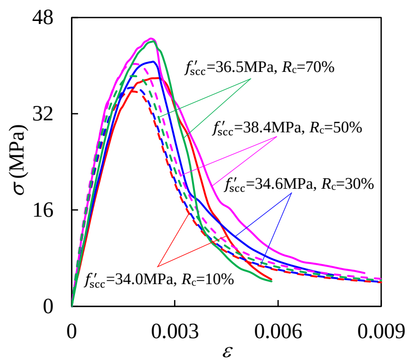

(d) Test of prisms [39]

Fig. 15. Comparison between the predicted and measured stress-strain curve of the SSC under compression.

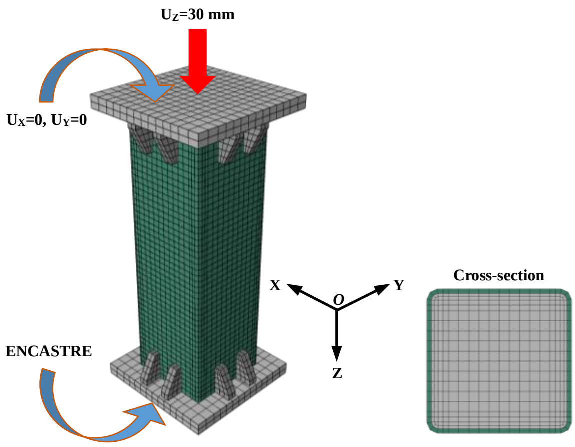

(a) Stub columns

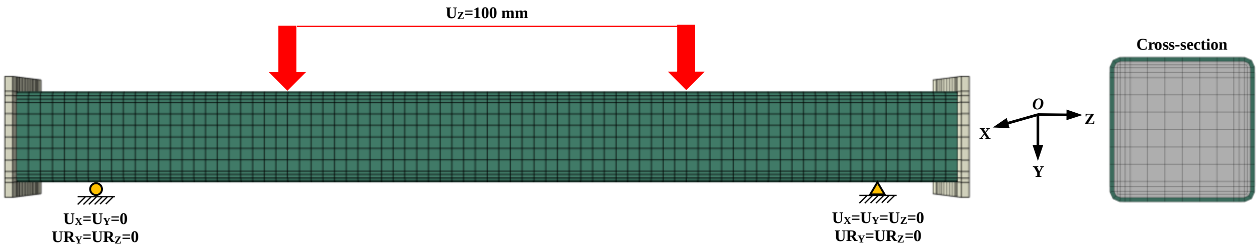

(b) Beams

Fig. 16. FE model of the SSC filled steel SHS specimens.

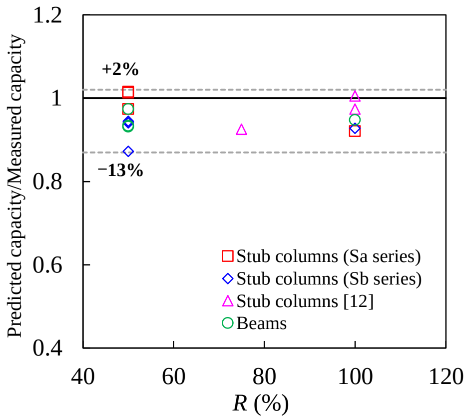

Fig. 17. The change in the ratio of predicted capacity to measured capacity of the SSC filled steel SHS specimens with respect to *R*.

Tables:

Table 1. Summary of experimental studies on the SSC filled steel tube members.

No.	Section type	Reserch contents	Role of steel slag products	Number of the specimens	References
1	Circular	Axial compressive behaviour of stub columns	SSCA and SSCA+SSFA	2	Yu et al. [12]
2		Axial and eccentric compressive behaviour of stub columns	SSFA	12	Yu et al. [13]
3		Axial compressive behaviour of stub columns	Cement	3	Wang et al. [14]
4		Interfacial bond property	SSCA+SSFA	12	Abendeh et al. [15]
5	Square	Axial compressive behaviour of stub columns	SSCA and SSCA+SSFA	3	Yu et al. [12]
6		Interfacial bond property	SSCA+SSFA	12	Abendeh et al. [15]

Table 2. Information of the stub column specimens.

No.	Label	B (mm)	t (mm)	L (mm)	B/t	R_c (%)	R_f (%)	$f_{cu,s}$ (MPa)	f_y (MPa)	K_s (MN)	R_{ks}	$N_{u,e}$ (kN)	F_n	$N_{u,fe}$ (kN)	$\frac{N_{u,fe}}{N_{u,e}}$
1	Sa-0-0	150	3.3	450	45.5	0	0	51.2	345.9	945.6	1.089	1911.0	1.000	1774.0	0.928
2	Sa-50-0	150	3.3	450	45.5	50	0	61.1	345.9	1055.6	0.993	1841.2	0.963	1792.8	0.974
3	Sa-100-0	150	3.3	450	45.5	100	0	61.9	345.9	1001.8	1.032	1958.7	1.025	1804.4	0.921
4	Sa-0-50	150	3.3	450	45.5	0	50	76.8	345.9	1091.4	0.982	2073.6	1.085	2106.5	1.016
5	Sa-50-50	150	3.3	450	45.5	50	50	76.8	345.9	973.3	1.067	2079.3	1.088	2106.5	1.013
6	Sb-0-0	150	4.6	450	32.6	0	0	51.2	398.9	1027.6	1.110	2392.5	1.000	2045.9	0.855
7	Sb-50-0	150	4.6	450	32.6	50	0	61.1	398.9	1062.2	1.091	2266.4	0.947	2141.8	0.945
8	Sb-100-0	150	4.6	450	32.6	100	0	61.9	398.9	1108.3	1.033	2325.3	0.972	2158.1	0.928
9	Sb-0-50	150	4.6	450	32.6	0	50	76.8	398.9	1069.5	1.104	2624.0	1.097	2468.1	0.941
10	Sb-50-50	150	4.6	450	32.6	50	50	76.8	398.9	1144.2	1.004	2827.1	1.182	2468.1	0.873

Table 3. Information of the beam specimens.

No.	Label	B (mm)	t (mm)	L (mm)	B/t	R_c (%)	R_f (%)	$f_{cu,b}$ (MPa)	f_y (MPa)	K_b (kN.m^2)	R_{kb}	$M_{u,e}$ (kN.m)	F_m	$M_{u,fe}$ (kN.m)	$\frac{M_{u,fe}}{M_{u,e}}$
1	B-0-0	120	3.5	1200	34.3	0	0	51.2	322.8	788.8	1.013	30.6	1.000	28.8	0.941
2	B-50-0	120	3.5	1200	34.3	50	0	61.1	322.8	764.7	0.979	30.5	0.997	28.5	0.934
3	B-100-0	120	3.5	1200	34.3	100	0	61.9	322.8	686.0	0.881	30.7	0.902	29.1	0.948
4	B-0-50	120	3.5	1200	34.3	0	50	76.8	322.8	683.6	0.872	31.1	1.016	29.0	0.932
5	B-50-50	120	3.5	1200	34.3	50	50	76.8	322.8	739.5	0.949	30.4	0.993	29.6	0.974

Table 4. Chemical compositions of steel slag and cement.

Compound		CaO	Fe_2O_3	SiO_2	Al_2O_3	MgO	MnO	P_2O_5	TiO_2	SO_3	Others
Content (%)	Steel slag	39.46	21.80	19.28	6.37	6.05	2.10	1.38	0.88	0.81	1.87
	Cement	62.72	3.44	21.32	5.44	1.76	0.01	0.10	0.24	2.60	2.37

Table 5. Physical properties of SSAs and natural aggregates.

Type	Apparent density (kg/m^3)	Bulk density (kg/m^3)	Water absorption rate (%)	Crushing index (%)	Fineness modulus
NCA	2718	1443	1.1	11.9 (Type II)	-
SSCA	3472	1806	1.7	5.7 (Type I)	-
NFA	2629	1440	2.5	-	2.34 (Zone II)
SSFA	3189	1926	5.0	-	2.98 (Zone II)

Table 6. Mix proportion and properties of concrete.

Type	R_c (%)	R_f (%)	Mix proportion (kg/m^3)								Property			
			Cement	Fly ash	Coarse aggregate		Fine aggregate		Tap water	WR	Slump (mm)	Spread (mm)	$f_{cu,28}$ (MPa)	E_c (GPa)
					NCA	SSCA	NFA	SSFA						
OC	0	0	398	170	770	0	795	0	204	2.35	270	645	46.3	32.3
SSC	50	0	398	170	385	385	795	0	204	2.35	280	660	57.7	33.2
	100	0	398	170	0	770	795	0	204	2.35	265	675	53.3	32.5
	0	50	398	170	770	0	398	398	204	2.35	260	710	64.3	34.3
	50	50	398	170	385	385	398	398	204	2.35	265	690	69.7	32.7

Note: WR=water reducer.

Table 7. Tensile properties of steel.

Type of specimen	Wall thickness (mm)	Yield strength (MPa)	Tensile strength (MPa)	Modulus of elasticity (N/mm^2)	Poisson's ratio	Elongation (%)
Stub column	3.3	345.9	423.1	1.89×10^5	0.264	14.2
	4.6	398.9	492.3	1.87×10^5	0.253	27.1
Beam	3.5	322.8	393.1	1.87×10^5	0.250	23.0

Table 8. Comparison between the calculated and measured capacities of the SSC filled steel SHS specimen.

Information of the specimens				Capacity	ACI 318-19 [25]		AIJ [50]		ANSI/AISC 360-16 [51]		EN 1994-1-1 [23]		GB/T 51446-2021 [52]	
Stub columns	No.	Label	ξ_{ssc}	N_{ue} (kN)	N_{uc} (kN)	$\frac{N_{\mathrm{uc}}}{N_{\mathrm{ue}}}$	N_{uc} (kN)	$\frac{N_{\mathrm{uc}}}{N_{\mathrm{ue}}}$	N_{uc} (kN)	$\frac{N_{\mathrm{uc}}}{N_{\mathrm{ue}}}$	N_{uc} (kN)	$\frac{N_{\mathrm{uc}}}{N_{\mathrm{ue}}}$	N_{uc} (kN)	$\frac{N_{\mathrm{uc}}}{N_{\mathrm{ue}}}$
	1	Sa-50-0	0.796	1841.2	1559.9	0.847	1559.9	0.847	1550.8	0.842	1716.9	0.932	1695.8	0.921
	2	Sa-100-0	0.785	1958.7	1571.8	0.802	1571.8	0.802	1562.7	0.798	1731.0	0.884	1709.1	0.873
	3	Sa-0-50	0.633	2073.6	1794.2	0.865	1794.2	0.865	1782.8	0.860	1992.6	0.961	1958.2	0.944
	4	Sa-50-50	0.633	2079.3	1794.2	0.863	1794.2	0.863	1782.8	0.857	1992.6	0.958	1958.2	0.942
	5	Sb-50-0	1.315	2266.4	1925.3	0.849	1925.3	0.849	1914.0	0.845	2076.7	0.916	2098.3	0.926
	6	Sb-100-0	1.298	2325.3	1936.8	0.833	1936.8	0.833	1925.4	0.828	2090.2	0.899	2111.5	0.908
	7	Sb-0-50	1.046	2624.0	2151.1	0.820	2151.1	0.820	2137.6	0.815	2342.4	0.893	2358.1	0.899
	8	Sb-50-50	1.046	2827.1	2151.1	0.761	2151.1	0.761	2137.6	0.756	2342.4	0.829	2358.1	0.834
	9	S3a*	0.935	1858.0	1763.9	0.949	1763.9	0.949	1755.2	0.945	1927.1	1.037	1927.3	1.037
	10	S3b*	0.935	1921.0	1765.8	0.919	1765.8	0.919	1757.1	0.915	1928.9	1.004	1929.4	1.004
	11	S4*	0.765	2235.0	1981.3	0.886	1981.3	0.886	1970.7	0.882	2183.6	0.977	2172.0	0.972
	Mean				0.854		0.854		0.849		0.935		0.933	
	Standard deviation				0.053		0.053		0.053		0.060		0.058	
Beams	No.	Label	ξ_{ssc}	M_{ue} (kN.m)	M_{uc} (kN.m)	$\frac{M_{\mathrm{uc}}}{M_{\mathrm{ue}}}$	M_{uc} (kN.m)	$\frac{M_{\mathrm{uc}}}{M_{\mathrm{ue}}}$	M_{uc} (kN.m)	$\frac{M_{\mathrm{uc}}}{M_{\mathrm{ue}}}$	M_{uc} (kN.m)	$\frac{M_{\mathrm{uc}}}{M_{\mathrm{ue}}}$	M_{uc} (kN.m)	$\frac{M_{\mathrm{uc}}}{M_{\mathrm{ue}}}$
	1	B-50-0	1.007	30.5	27.3	0.895	23.0	0.754	23.0	0.754	26.7	0.875	25.9	0.849
	2	B-100-0	0.994	27.6	27.1	0.982	23.0	0.833	23.0	0.833	26.6	0.964	25.5	0.924
	3	B-0-50	0.801	31.1	27.6	0.887	23.0	0.740	23.0	0.740	26.9	0.865	26.4	0.849
	4	B-50-50	0.801	30.4	27.9	0.918	23.0	0.757	23.0	0.757	27.1	0.891	26.8	0.882
	Mean				0.921		0.771		0.771		0.899		0.876	
	Standard deviation				0.043		0.042		0.042		0.045		0.036	

Note: *, the data are from Yu et al. [12].